This is a preprint, the final version is subject to change, of the American Mineralogist (MSA)
Cite as Authors (Year) Title. American Mineralogist, in press.
DOI: https://doi.org/10.2138/am-2019-6629

REVISION I

Intragranular plasticity vs. grain boundary sliding (GBS) in forsterite: microstructural evidence at high pressures (3.5- 5.0 GPa)

Caroline Bollinger[(1)(2)]*; Katharina Marquardt[(1)(3)]; Filippe Ferreira[(1)]

[(1)] Bayerisches GeoInstitut, Universität Bayreuth, 95445 Bayreuth, Germany

[(2)] Now at: Department of Earth and Planetary Sciences, Washington University in Saint Louis, Saint Louis, Missouri, USA.

[(3)] Now at: Imperial College London, Department of Materials, Faculty of Engineering, London, UK

*corresponding author: c.bollinger@email.wustl.edu

This is a preprint, the final version is subject to change, of the American Mineralogist (MSA)
Cite as Authors (Year) Title. American Mineralogist, in press.
DOI: https://doi.org/10.2138/am-2019-6629

ABSTRACT

The plasticity of the mantle is still not well constrained and satisfactory mineral physics-based rheological laws are still missing. Despite olivine being the major component of the upper mantle, it is still debated, which deformation mechanism (dislocation creep, diffusion creep, grain boundary sliding) dominates deformation. High-pressure research developments (state-of-the-art presses, synchrotron experiments…) as well as competitive analysis utilities (software analysis, microscopy…) allow considering intra- and intergranular mechanisms (grain boundary sliding accommodated by diffusion/dislocation creep) simultaneously. To study the contribution of individual deformation mechanism to the overall deformation in the upper mantle, we deformed polycrystalline forsterite at 3.5 - 5.0 GPa, 1000 °C - 1200 °C, $2x10^{-5}s^{-1}$ at different strains in a 6-axis Mavo press. Split cylinder experiments allowed to characterize an 'internal' surface of the sample before and after the deformation experiments. Intra- and intergranular deformation was tracked using a focus ion beam milled reference grid on this surface. Grain internal misorientation where obtained from Electron Backscatter Diffraction (EBSD) data. Both techniques suggest the dominance of intragranular deformation, in agreement with the fact that the samples have been deformed in the dislocation creep regime, as usually defined. Moreover, strain markers and out-of-plane displacements of grains provide the first microstructural evidence for a contribution of grain boundary sliding to plastic deformation at upper mantle pressure. Whether these displacements are grain boundary sliding or involve grain boundary migration cannot be clarified, given the resolution of the strain markers. Our EBSD data suggest that grain boundary processes become increasingly relevant at temperatures above 1100 °C and ensure homogenous plastic strain distribution in the aggregate.

Keywords: forsterite, crystal slip plasticity, grain boundary sliding, EBSD, deformation.

This is a preprint, the final version is subject to change, of the American Mineralogist (MSA)
Cite as Authors (Year) Title. American Mineralogist, in press.
DOI: https://doi.org/10.2138/am-2019-6629

INTRODUCTION

Flow in the mantle is directly related to plate tectonics, orogenesis, subduction, and volcanic eruptions. Thus, understanding mantle flow is essential for characterizing the dynamics of the Earth. Olivine represents 60% of the upper mantle (e.g., Nicolas and Poirier, 1976; Bai et al., 1991; Mackwell, 1991), and exhibits a strong elastic and plastic anisotropy (e.g., Poirier, 1985; Nicolas and Christensen, 1987; Mainprice and Silver, 1993; Walid Ben Ismaïl David Mainprice 1998; Mainprice et al., 2000; Hansen et al., 2012a). Consequently, observations of seismic anisotropy can be used to interpret flow directions in the mantle (*e.g.*, Nicolas et al., 1973; Vinnik et al., 1984; Nicolas and Christensen, 1987; Silver and Chan, 1988; Mainprice and Silver 1993; Russo and Silver, 1994; Vauchez and Barruol, 1996; Karato et al., 2008). Indeed, seismic anisotropy is strong in the upper mantle and decreases down to the transition zone (e.g., Christensen 1984, Nicolas and Christensen 1987, Montagner and Tamimoto, 1991, Ben Ismail and Mainprice, 1998, Debayle et al., 2005). From the shallow to the deeper parts of the upper mantle, pressure and temperature (P, T) increase and the deformation controlling mechanism of olivine changes. This results in the formation of different crystal preferred orientations (CPO) or in the destruction of the CPO (Mainprice et al., 2005), which may affect seismic anisotropy. The deformation mechanisms that were studied most intensely are dislocation creep (e.g., Karato and Wu, 1993, Couvy et al., 2004), disclination-accommodated dislocation creep [(Cordier et al., 2014; disclinations were identified in samples deformed experimentally by Demouchy et al. (2012, 2014)], grain boundary sliding (GBS - Goldsby and Kohlstedt, 2001; Karato, 2008), elastically accommodated grain-boundary sliding (Jackson et al., 2013), and grain boundary sliding accommodated by dislocation creep

(DisGBS - Hirth and Kohlstedt, 1995 a, b, 2003, Hansen et al., 2012b) as well as diffusion creep (e.g., Miyazaki et al. 2013).

The rheological laws consider the contribution of each independent mechanism. The total stain rate ($\dot{\varepsilon}$) can be calculated as (e.g., Warren and Hirth, 2006):

$$\dot{\varepsilon} = \dot{\varepsilon}_{Dis} + \dot{\varepsilon}_{Diff} + \dot{\varepsilon}_{GBS} + \dot{\varepsilon}_{LTP} \qquad (1)$$

with $\dot{\varepsilon}_{Dis}$ the strain rate for dislocation creep, $\dot{\varepsilon}_{Diff}$ the strain rate for diffusion creep, $\dot{\varepsilon}_{GBS}$ the strain rate for GBS accommodated by diffusion/dislocation creep, and $\dot{\varepsilon}_{LTP}$ the strain rate resulting from low temperature (<900 °C, *e.g.*, Warren et al. 2006) plasticity. The deformation maps drawn from this general flow law are based on empirical rheological datasets of polycrystalline aggregates and single crystal mechanical properties. They describe the phenomenological viscoplastic behavior of olivine. The mechanism with the fastest strain rate controls deformation, *e.g.,* diffusion (*e.g.,* Karato et al., 1986; Karato and Wu 1993) or dislocation creep (*e.g.,* Kohlstedt and Goetze, 1974; Weertman and Weertman, 1975). Grain boundaries (GB) processes were commonly ignored as it was assumed that they contribute only very little to overall deformation. Until recently, no microstructural work has been performed to describe the processes in aggregates deformed close to two different regimes.

Crystalline plasticity (dislocation creep) is usually considered to be the main CPO producing mechanism (Karato and Wu, 1993; Kohlstedt and Goetze, 1974; Tommasi et al., 2000; Mainprice et al., 2005; Castelnau et al., 2010; Raterron et al., 2014). In contrast, olivine deformed dominantly in diffusion creep (*e.g.*, Karato et al., 1986; Karato and Wu, 1993; Miyazaki et al., 2013) can also produce CPO. These studies have been performed at ambient confining pressure in very fine-grained forsterite resulting in debates of the applicability to realistic P T conditions of flow in the Earths mantle.

Dislocation and diffusion creep have been studied experimentally for about half a century. GBS, DisGBS and GBS accommodated by diffusion creep have only recently gained more attention as they seem to play a crucial role during deformation. Hence, contributions of grain-boundary networks such as grain boundaries and triple junctions to rock deformation in the dislocation creep regime are not well understood. The development of different textures in olivine assemblages is usually attributed to changes in the dominant slip system activity inside grains in response to changes in pressure, temperature, stress and water content (*e.g.*, Jung et al*.,* 2006). The change of slip systems is thought to also influence the rheology considerably (*e.g.*, Raterron et al., 2014).

However, some studies demonstrate that even in a "well-defined" deformation regime (as expressed by rheological laws), a variety of different mechanisms must operate simultaneously to fully describe the rheology of an aggregate (*e.g.*, Dimanov et al., 2011). Recent experiments on olivine suggest that not only intragranular plasticity but also relative displacement between adjacent grains account for the overall deformation. Several studies (Hirth and Kohlstedt, 1995a, b, 2003; Kohlstedt and Wang, 2001; Ter Heege et al*.,* 2004; Warren and Hirth, 2006; Warren et al*.,* 2008; Zhao et al., 2009; Hansen et al., 2011, 2012b; Tasaka et al., 2013, 2016; Ohuchi et al., 2015; Maruyama and Hiraga, 2017a,b) have particularly emphasized the existence of a deformation regime with linear stress sensitivity and grain size dependence, consequently attributed to GBS. Hence, GB seem to play an essential role in deformation of polycrystalline olivine and GBS might be an important deformation mechanism in addition to diffusion and dislocation creep in the Earth's mantle.

Consequently, the present study focusses on GB processes at relevant P and T conditions. We examine microstructural features to evaluate the activation of different deformation mechanisms in forsterite deformed at 5.0 GPa and temperatures from 1000 to 1200 °C in the dislocation creep

regime. We present techniques developed to engrave strain markers on olivine surface which are preserved after high-pressure, high-temperature (HP-HT) deformation and allow Electron Backscatter Diffraction (EBSD) acquisition in order to characterize the contribution of grain boundary mobility in olivine compared to crystalline plasticity.

EXPERIMENTAL

Preparation of the starting material

Forsterite has been synthesized from MgO (99.99% purity with 1.5 µm grain size) and SiO_2 (99.99% purity with ~150 µm grain size) oxide powders from ChemPur. The powders were mixed together in an alumina mortar with ethanol. MgO was added in excess to avoid the formation of enstatite during synthesis since MgO powders easily captures humidity from the air during the weighing. This mixture was then sintered in a furnace at 1500 °C for at least 12 hours and ground out again. This procedure has been repeated five times. The evolution to 100% forsterite was monitored with X-rays diffraction and confirmed later in the study. Once forsterite was formed, the MgO in excess was removed using acetic acid at 10 % at 60 °C (this process was repeated four times). The resulting forsterite powder was then sent to PNF^2 (CIRIMAT, Toulouse, France) to be aggregated and densified by flash sintering (Guignard et al., 2011). This resulted in pellets of 2 cm high and 4 cm in diameter. The starting microstructure of the aggregate has been analyzed with a Scanning Electron Microscope (SEM) and EBSD before deformation. The grain size was found to be between 20 and 100 µm with a lognormal distribution. The grains are randomly orientated with straight grain boundaries. Their shape is rather equiaxed with a mosaic texture.

For deformation experiments, cylinders (1.5 mm in diameter and length) were cored in the middle part of the pellet. The cylinders were then cut in two halves. The face of one halve was carefully

polished for EBSD mapping and strain markers are milled (section 2.2) before the deformation experiment. The second half was prepared for EBSD after the deformation experiment (section 2.4).

Preparation of a reference grid in a split cylinder

We used the split-cylinder technique (fig. 1a; *e.g.*, Raleigh, 1965; Peach and Spiers, 1996; Xu and Evans, 2010; Quintanilla-Terminel et al*.,* 2016, 2017) to create a surface inside the sample where investigation of local strains and microstructure could be performed. A grid was milled (fig. 1b) as a strain marker on one of these internal surface using the focus ion beam (FIB) Scios using a 30 kV Ga-beam at 30 nA. The design of the grid is described in figure 1b. We used a groove depth of 7.5 μm and 100 nm width, resulting in a 25 μm² square grid. Additionally, we performed some experiments with different grids, *e.g.,* M585 that has 75 and 100 μm² squares. The milling of the grid leads to deposition of gallium on the surface that is difficult to remove without polishing and which prevents the formation of high-quality Kikuchi patterns for EBSD mapping. To overcome this issue we protected the surface by depositing of a thin layer (~200 nm) of polymer (Poly(methyl methacrylate), PMMA) using a photolithography technique (e.g. Quintanilla-Terminel et al*.,* 2016) before the milling. After milling, the protecting layer was removed by letting the sample for 15 min in acetone at 40° followed by a slight polish with 0.25 μm diamond powder. After this procedure, EBSD characterization was possible. For the deformation experiment, the half-cylinders were put together again with a thin slice (<150 μm) of NaCl in between to avoid surface adhesion of the two parts (fig. 1c).

Deformation

The split-cylinder was inserted in a molybdenum capsule with a 25 µm thick wall. In the high-pressure deformation assembly, the sample was placed between alumina pistons (hard alumina and crushable alumina on top of each other - fig. A in the *Supplementary Material*). Above the sample, hard alumina with four holes was used for the D-type thermocouple. An MgO sleeve surrounded this column to provide insulation of the sample from the graphite step-furnace, used to reduce the temperature gradient. This furnace and inner parts were inserted in a ZrO_2 sleeve as thermal insulator with two MgO rings on each side. All those parts were loaded in an 8 mm-unfired pyrophyllite cube.

The assembly was then placed between the six second-stage anvils with 6-mm truncation to apply the confining pressure to the cube in the six-ram MAVO press (Manthilake et al., 2012). The pressurization occurred in approximately 90 min, followed by power-controlled heating within 30 min. After reaching the desired P/T conditions, annealing was performed for ~30 min to let the system adjust the experimental conditions and equilibrate potential microstructures introduced during cold compression. One pair of rams was then pushed forward by injecting oil at a rate corresponding to an applied strain rate of $\sim 2x10^{-5}s^{-1}$. Another pair of rams remains fixed as the last one was pushed backward in response to insure a constant confining pressure while the sample was deformed in pure shear geometry. The applied pressure range was 3.5 to 5.0 GPa with a temperature range from 1000 to 1200 °C. The applied strain range was 10 to 40%, leading to a deformation duration of 3 to 5 hours. The temperature was monitored with the thermocouple. After deformation, the sample was quenched by switching off the power, and pressure was released slowly over 12 to 18 hours. The summary of the experimental conditions is reported in Table 1.

Post-deformation preparation and EBSD analysis

After deformation, the complete assembly was mounted in Epofix® and then ground to the capsule from top and bottom. This leads to the dissolution of the salt slab placed between the halves of the cylinder and permitted us to cut the assembly at the right place in order to open the capsule like a book, exposing both surfaces of the split-cylinder.

The recovered sample was then remounted in Epofix® to be properly cleaned for SEM imaging and EBSD: the surface with the grid was cleaned with ethanol and acetone before imaging. When necessary, a smooth polish with 0.1 alumina and, in rare occurrences, with 0.25 µm diamond powder solution was applied before EBSD mapping to reach some areas of the recovered sample that were not possible to be observed initially. We refrained from more re-polishing the sample after the experiment to observe the same surface before and after deformation. Additional polishing would remove at least a 50 µm layer and would hence preventing this endeavor.

The face with no grid was prepared with the complete procedure for an EBSD quality polish*, i.e.* starting with grinding paper 1200 to 4000 grit and finished with 0.25 µm diamond powder solution and with a colloidal silica suspension polish. We removed a layer of 100 to 150 µm. This surface, used as a reference, is considered to be representative for the bulk sample and is refined to later as the bulk. This procedure enables us to compare observations of bulk behavior to observation made at the split-cylinder surface and consequently prove absence or presence of surface effects potentially caused by the contact with the thin salt-layer (see section Results).

To collect the EBSD maps before deforming the forsterite (orthorhombic, *Pnma*) aggregates, we used a ZEISS Leo Gemini 1530 Schottky FE-SEM operated at an accelerating voltage of 20 keV and a probe current of about 2.0–2.5 nA (60 mm aperture and high current option). We collected data on a square grid using the software package of Oxford Instruments (HKL Channel 5) and a

NordlysS camera from Oxford Instruments with a CCD resolution of 1344 × 1024 × 12 bit. The pattern were reduced to a binned pattern size of 4×4 and a timing per frame of 24 ms. After the deformation, we used the dual beam-FIB.

The EBSD analyses for the deformed samples were performed using the FEI Scios FEG dual beam machine (FIB). It is equipped with EDAX-TSL Digiview IV EBSD Detector. The OIM Analysis (Orientation Imaging Microscopy Analysis) software, from EDAX, is included in the TEAM 8 user interface of the EBSD system and was used to record the electron backscatter diffraction patterns (EBSP) after background correction. EBSPs were acquired with a binning of 9×9, the Hough pattern size was 120 at a theta angle step size of 0.5°. The step size of the map can influence the Kernel average misorientations (KAM) distribution (Wright et al., 2011; see also below for details), thus we always used the same step size of 2.8 μm to record all maps (before and after deformation). For EBSD map analyses the HKL Channel5 maps were converted to a hexagonal grid and processed using OIM Analysis.

No diffraction patterns were saved for the dataset acquired using the ZEISS SEM. The data collected at FIB included the EBSPs stored in a single .hdf5 data file. Storage of the EBSPs allows post processing, such as re-indexing (Marquardt et al., 2017). We used the Neighbor Pattern Averaging and Re-indexing (NPAR, Wright et al., 2015) function where pattern of one point in a scan are averaged with the patterns of the six neighboring scan points, in our case of a hexagonal grid. This results in an effective smoothing of the information and a reduction of the spatial resolution, as pointed out by Marquardt et al. (2017). Note that we congruously used the raw dataset to study the KAM distribution (Wright et al., 2015).

Data treatment also includes the application of a pseudo symmetry correction for the (100) system of the olivine and a grain dilation correction of 10 pixels. The group of pixels below a size of 10 points within 3 rows was excluded (Marquardt et al., 2015 – see figure 2 and next section).

EBSD allows comparing the location of the grains before and after the deformation and eventually a change of shape or of crystal orientation. To be able to detect more deformation details in the microstructure, it is advised to use more information that covered by the inverse pole figure color-coding alone. The tools used here are implemented in OIM Analysis v8. It is also provided in the open source MATLAB toolbox MTEX (http://mtex-toolbox.github.io/ - Hielscher and Schaeben, 2008). To better understand intragranular deformation of olivine, we used the following methods:

- the KAM, which calculates the average misorientation between a pixel *i* and its neighbors. It highlights the local strain gradients from misorientations, such as subgrains boundaries or geometrically necessary dislocations. Only the first neighbor kernels are analyzed here.
- the Grain Reference Orientation Deviation (GROD) is based on the misorientation between a reference point (e.g., the mean orientation, mis2mean). It shows the local deformation within individually grains compared to the mean orientation of the considered grain.

RESULTS

Deformation experiments were not performed at a synchrotron beamline, with no in situ access to the stress. The PT conditions applied here correspond to those usually attributed to the dislocation creep regime (for example, Bollinger et al., 2015; Ohuchi et al. 2015). The compression direction is horizontal.

Grain boundary mobility

Sample M611 (3.5 GPa; 1000 °C; 15%) shows the sample before and after the deformation (figure 2). The black frame corresponds to the area recovered after the experiment. The milled grid allows to recognize the region of interest and to track individual grains (fig. 2a, b). The EBSD data before deformation is presented in figure 2c, and figure 2d shows the EBSD map after deformation. The grid and the EBSD maps permit to track deformation accommodated by individual grain boundaries. Additional examples are given in the supplementary material (fig. B and C).

Evidence from the markers. The grid was used as a strain marker (fig. 2) and allows to track displacement at grain boundaries, caused by grain boundary sliding and possibly if shear strain is coupled with grain boundary migration. The latter aim proved to be out of reach at the current methodological level. The difficulty in preserving strain markers after HP-HT experiments has led us to engrave relatively wide (about 100 nm) lines. It stands to reason that these wide markers limited the detectability of the potential presence of grain boundary migration associated with shear. Evidence for in-plane offsets of grain boundaries were limited, which is related to quenching from HP-HT deformation conditions. This process results in decohesion of a large fraction of grain boundaries (see example on figure 2, 3e, f, g) that are thus inappropriate for offset evaluations. We observed however in-plane displacements at grain boundaries clearly marked by strain markers offsets (figure3).

Some exemplary areas before (used as reference) and after deformation are shown for samples M582 deformed at 5.0 GPa – 1000 °C (fig. 3a, b, c) and M585 (5fig. 3d, e) deformed at 5.5 GPa – 1050 °C, and after deformation for M615 (fig. 3f, g) deformed at 3.5 GPa - 1200 °C. Tracking changes in the position of the grid before and after deformation reveals that the lines are mainly

segmented at grain boundaries creating offsets. This is indicated by black arrows. The markers travers the grains un-interrupted. However, in the vicinity of the grain boundary, relative displacement between the grains is documented by the markers. The offsets of the strain marker are in the range of 1 to 6 μm for all the experiments. The experimental conditions do not seem to have an impact on the amount of the displacements.

A remarkable offset of 6 μm is shown on figure 3c and indicated with white arrows. This observation has been made in several occasions. Of all observations, three show a bending of the marker close to the grain boundary instead of an offset (figure 3f, gray arrow in the white circle). The right grain, surrounded by a white circle was rotated counterclockwise as indicated by the marker inside. Despite such rotations have been observed for several grains, neither the rotation angle nor the frequencies of full grain rotations can be quantified or statistically evaluated with respect to any specific experimental conditions.

Evidence for out-of-plane displacement. The main displacements at grain boundaries is caused by out-of-plane translations visible with secondary electron (SE) images (fig. 3f, 4). When a ledge is formed at the surface of a sample, it represents a location where SE emission and capture by the detector is strongly affected, giving rise to a strong white (toward the detector) – black (direction opposite to the detector) contrast. Our images show pervasive evidence for such displacements.

In fig. 3f a grain that appears to have popped out of the sample is indicated with the white arrow. This grain additionally shows slight offsets and a slightly counterclockwise rotation. With the reasonable assumption that the surface of the sample was perfectly flat before the experiment, this grain reminds us of a horst in a horst-and-graben structure.

Qualitative observation of this out-of-plane displacement are shown on figures 3e and 4. Some grains popped up while some others are slightly pushed down by surrounded grains. Those pushed up grains are then freer to rotate on the axis perpendicular to the rotation axis, often leading to a surface tilting. We did not note any new grains when comparing before and after pictures, nor any indicative changes of shape. Comparing the EBSD map before and after helped to track up- or down-pushed grains leading to a change of size in the image (the grain might appear smaller when it is pushed away from the camera and reversely). Note that discrete changes of the grain size might also be related to slight polishing of post-experimental samples.

Intragranular plasticity

Deformation of the strain markers within the grains is rarely observed, independent of the overall plastic strain. Since our procedure is able to preserve the sample surface for EBSD analyses after deformation, we have investigated the intragranular plasticity from the study of misorientations. An example of such measurements on a sample deformed at 1000 °C (M640) is depicted in figure 5. The KAM (fig. 5a, b) and the GROD (fig. 5c, d) of samples before and after the experiments are displayed. The GROD shows how misorientation gradients build up at the scale of the grains. During plastic strain (ε_p), orthorhombic olivine polycrystals builds up very strong misorientation gradients and heterogeneities. Lattice rotations are more evident (higher GROD values) near triple junctions and grain boundaries while the GROD values decrease inside the grains (Figure 6). This indicates strain heterogeneities inside grains and is common observation at all temperatures between 1000 °C and 1100 °C at 5.0 GPa (fig. 6a, b, c, samples M582 and M575) and at 3.5 GPa (fig. 6d, sample M611). We see that less heterogeneities developed at 1200 °C (fig. 7) at 3.5 GPa (M615) and 5.0 GPa. (M621).

Further quantification to compare samples is limited by the grain-based nature of the GROD, which may thus be affected by grain size. Instead the KAM, which probes local gradients of deformation and it is sometimes used as a proxy for geometrically necessary dislocation density or plastic strain (e.g., Rollett et al., 2012), was used.

The GROD observations can be correlated with the KAM to highlight the formation of subgrain boundaries, sometimes to the point of forming a new grain, *i.e.* creating a high angle boundary. Finally, the KAM distribution is not always localized near the grain boundaries which moved but remains rather heterogeneous. The KAM of sample M640 is shown in Figure 5, which exemplifies the activity of intragranular plasticity caused by sample deformation. Since the KAM is a local measurement of misorientation, one can plot the KAM distribution to compare samples. An example of the evolution of the KAM distribution in the same sample (M621) before and after deformation is shown on figure 8. After deformation, the KAM distribution spreads and shifts to larger misorientations, typically in M621 (fig. 8) from an initial maximal misorientation of 0.25° to 0.45° for the bulk and the surface after deformation, respectively. This reflects heterogeneities developed in the sample after plastic strain. Note that we have duplicate EBSD measurements for some samples on a surface not exposed during deformation (representative of the bulk). The KAM distribution in the bulk is identical to the one measured on the internal surface of the split cylinder (max 0.45° for both – fig. 8).

At 3.5 GPa and 1000 °C, the maximum of KAM distribution is 0.54 (table 2) for experiment M611 (fig. D. a). For two experiments at 1200 °C (M606 and M615) this value does not change (0.54 and 0.53, respectively). The full width at half maximum FWHM as a function of the temperature is

plotted in supplementary figure D.b. It is about 0.79 at 1000 °C (table 2) and varies between 0.55 and 0.73 at higher temperature.

The KAM distributions of all samples after deformation at 5.0 GPa are plotted simultaneously in figure 9a. Besides small differences, the samples can be sorted into two groups related to the deformation temperature: 1000-1100 °C and 1200 °C (see table 2 for details). Below 1200 °C, the KAM distribution ranges 0.54° to 0.95°. Above 1100 °C, the KAM heterogeneities are less with the KAM distribution ranging from 0.45° to 0.54°. The full width at half maximum (FWHM) as a function of the temperature is plotted on figure 9b. This value is in the range of 0.86° to 1.28° at temperatures up to 1100 °C and significantly decreases to 0.66°-0.61° at 1200 °C.

The toolbox MTEX was used to evaluate if the KAM shows a relation to grain size, as suspected because smaller grains that present a higher interface to volume ratio (Kumamoto et al., 2017). This is plotted for samples deformed at 5.0 GPa over the full temperature range (see figure 10 for details). For sample M585, the KAM distribution is compared before and after the deformation experiment. For all samples, one observes, as for M585, that the KAM remains below ca. 1° whatever the size of the grain. After the deformation, the distribution spreads above 1.5°, showing the development of heterogeneities of the plastic strain. Below 1200 °C, the small grains (i.e., < 60 µm) tend to develop a higher KAM as can be seen for M582 and M585: the KAM can be up 3 to 4° (33% and 29% of the small fraction is above 1.5°), whereas the maximum varies between 2° and 3° for larger grains (30 and 28% of the grains above 60µm size). At 1200 °C the maximum KAM reaches about 2.4° (M628 – 16% of the small fraction and 12.5% of the big grains) and the distribution is rather constant with no clear maximum related to the grain size distribution. We observe throughout all the data that almost 28% of both of the fraction grain size are above 1.5°

misorientation below 1200 °C as those values decrease to an average of 15 to 12% at 1200 °C and 5GPa. At 3.5 GPa and 1000 °C, we see that the small grains have a maximum of 2.5° for 20%, and 20% of the big grains have a 2° misorientation. At 1200 °C, the misorientations differ from 2 to 1.5° with 10% of the small fraction vs. 9% of the bigger grains.

DISCUSSION

The offsets and the out-of-plane displacement are robust indicators of grain boundary sliding. The rare occurrences of bending of the grid is the evidence of GBS in conservative grain boundary migration as mentioned in Maruyama and Hiraga (2017a). This is an intriguing observation, because the experiments are performed in dislocation creep accommodated by grain boundary sliding (Ohuchi et al. 2015). High offset of the marker at the grain boundary are observed occasionally (fig. 3c). The relative rarity of observations might be caused by either grains not orientated to be plastically deformed by dislocation creep or the stress applied is not high enough. Second, the spacing between the lines (in the best cases, 25 μm) of the grid is too large and several local displacements are not observed. This limits the trackability and measurability of possible grain boundary migration. In future studies we recommend grid spacings of 1μm or less, which might however be restricted by FIB time.

We can neither prove or exclude the occurrence of GBM at high pressure, but evidence for GBS was observed. GBS and dislocation creep acting simultaneously is evident from the presented data. Minor contributions of other mechanisms are not excluded.

The out-of-plane displacements with rotation observed in this study, in the DisGBS regime at 3.5-5.0 GPa, is in agreement with the observations of Maruyama and Hiraga (2017a) at 1 atm. Particularly, the horst-and-graben structures where individual grains have more freedom of rotation

are very similar. However, neither EBSD nor high strain occasionally applied on the sample allowed the observe any particular grain switching events as described by Maruyama and Hiraga (2017a). Our observations at high pressure are to some extend comparable to their study, as the surface in contact with salt may result in free-surface effects despite having been performed at high confining pressure. The out-of-plane grain displacements are nevertheless supportive of active grain boundary sliding during deformation from 1000 °C.

The local gradients of deformation indicated by the variation of the KAM is identical whether observed for the bulk or the split-cylinder surface. We conclude that at the scale of the KAM measurement, the split-cylinder technique induces no artifact for this evaluation.

Comparing the heterogeneities of the deformation measured at two different pressures reveals that the KAM distribution maximum (and so the FWHM) at 3.5 GPa is lower than at 5.0 GPa at 1000 °C (table 2). It does not change at 1200 °C and low pressure while it decreases at 5.0 GPa. The differences in the heterogeneities at two different temperatures is much less visible at 3.5 GPa than at 5.0 GPa (fig. D. b). At 5.0 GPa, since there is no transition in deformation mechanisms and dislocation activity in the temperature range of this study in forsterite, and since we have shown that the KAM heterogeneities are mostly related to the difficulty in transferring plasticity from one grain to another, we propose that at 1200 °C an increase in the grain boundary activity is responsible for this evolution. Further experiments need to be performed at 3.5 GPa to have better statistics to conclude if there is also an effect of the temperature on the activation of grain boundaries at such experimental conditions.

As Hirth and Kohlstedt (2003) already suggested, grain boundaries slide, allowing intragranular plasticity to occur in DisGBS regime. Ohuchi et al. (2015) conclude that the CPO observed is due to both mechanisms (GBS and dislocation creep) and proposed a rheological law for this specific regime. Our experiments have been performed in P - T conditions comparable to those applied by Ohuchi et al. (2015). Consequently, it is reasonable to consider that they have been performed in the lower bound of the dislocation creep regime (e.g., Warren et al., 2006). This is consistent with our microstructural observations; therefore we support the thesis of Hirth and Kohlstedt (2003) and Ohuchi et al. (20151).

Tielke et al. (2016) show that the strain rate for olivine aggregates in the dislocation creep regime is due to intracrystalline plasticity with a grain size sensitive mechanism acting at the same time. This is also concordant with our results, where the smallest grains show more misorientations than the larger grains. Nevertheless, we are not able here to establish the relative contribution to the plastic strain of each mechanism involved in the plastic deformation of forsterite.

Maruyama et al. (2017 a, b) used a very fine resolution for the milled-grid (1 μm-spacing) as strain marker at the surface of their samples. The samples were fine grain (1 μm) forsterite + diopside aggregates deformed in the diffusion creep regime. They showed the first microstructural evidences of grain boundaries mobility at room-pressure and high-temperature: i.e. grain boundary migration, grain boundary sliding, rigid body grain rotation, and grain neighbor switching. Here we use a larger spaced-grid (25 to 75 μm) with bigger grain size (20 to 100 μm) of pure forsterite aggregates. The sample have been uniaxially deformed at 3.5-5.0 GPa and 1000 °C to 1200 °C. For the first time we show microstructural evidences of grain boundaries sliding at P and T relevant for the Earth's mantle. The resolution related to our grit does not allow to prove the presence or absence

of GB migration. In future studies it may however be possible to measure the shear strain induced by the mobile grain boundaries (Molodov et al., 2011a, b).

IMPLICATIONS

Implications of this study are two-fold. From the technical point of view, we present methodological developments, that allow the usage of the split-cylinder technique to extract information of the deformation mechanisms from an internal surface in a polycrystalline olivine aggregate. We present the first study at high pressure that uses strain markers and observation of the internal surface to infer grain boundary sliding as well as EBSD-based intragranular misorientation measurements. This allows to assess plastic strain heterogeneity in deformed forsterite aggregates at high pressure and temperature. The development of such approaches is important to provide further quantitative data, which could be used in refining plasticity models. Further work is needed to increase resolution in order to detect possible grain boundary migration and to obtain more quantitative data about sliding, migration and the induced shear strain.

Concerning the rheology of olivine, we provide the first experimental evidence of grain boundary sliding at high-pressure. Our work is an important step forward and provides constraints on grain boundary sliding accommodated by dislocation creep, an essential mechanism required to describe the rheology of olivine in the upper mantle.

ACKNOWLEDGMENTS

CB gratefully thanks Prof. M. Lippitz, Chairholder and P. Knödler from the Chair for Experimental Physics III - Ultrafast Nanooptics, Universität Bayreuth, for the polymer deposit on the sample's surfaces. The grids were milled with the FIB Scios supported by the DFG grant INST 91/315 – 1

FUGG. Financial support granted to K.M through the German science foundation (DFG, MA 6287/6) to supported the EBSD detector on the FIB and the position of F.F.. This project was supported by the German Alexander von Humboldt Foundation and the Free State of Bavaria. This work would not have been possible without the technical skills of H. Fischer, R. Njul, H. Schulze and S. Übelhack.

REFERENCES CITED

Bai, Q., Mackwell, S. J., and Kohlstedt, D. L. (1991) High-Temperature creep of olivine single crystals: 1. Mechanical results for buffered samples. Journal of Geophysical Research 96 (B2), 2441-2463.

Ben Ismail, W., and Mainprice, D. (1998) An olivine fabric database: An overview of upper mantle fabrics and seismic anisotropy. Tectonophysics, 296, 145-158.

Bollinger, C., Merkel, S., Cordier, P., and Raterron, P. (2015) Deformation of forsterite polycrystals at mantle pressure: Comparison with Fe-bearing olivine and the effect of iron on its plasticity. Physics of the Earth and Planetary Interiors, 240, 95–104.

Castelnau, O., Cordier, P., Lebensohn, R.A., Merkel, S., and Raterron, P. (2010) Microstructures and rheology of the Earth's upper mantle inferred from a multiscale approach. Comptes Rendus de Physique 11, 304-315.

Christensen, N.I. (1984) The magnitude, symmetry and origin of upper mantel anisotropy based on fabric analysis of ultramafic tectonics. Geophysical Journal of the Royal Astronomical Society banner, 76, 89-112.

Cordier, P, Demouchy, S., Beausir, B., Taupin, V., Barou, F., and Fressengeas, C. (2014) Disclinations provide the missing mechanism for deforming olivine-rich rocks in the mantle. Nature 507, 51-56.

Couvy, H., Frost, D. J., Heidelbach, F., Nyilas, K., Ungár, T., Mackwell, S., and Cordier, P. (2004) Shear deformation experiments of forsterite at 11 GPa - 1400 °C in the multianvil apparatus. European Journal of Mineralogy, 16 (6), 877-889.

Debayle, E., Kennett, B., and Priestley, K. (2005) Global azimuthal seismic anisotropy and the unique plate-motion deformation of Australia. Nature 433, 509-512.

Demouchy, S., Tommasi, A., Barou, F., Mainprice, D., and Cordier, P. (2012) Deformation of olivine in torsion under hydrous conditions. Physics of the Earth and Planetary Interiors, 202-203, 57-70.

Demouchy, S., Mussi, A., Barou, F., Tommasi, A., and Cordier, P. (2014) Viscoplasticity of polycrystalline olivine experimentally deformed at high pressure and 900 °C. Tectonophysics 623, 123-135.

Dimanov, A., Raphanel, J., and Dresen, G. (2011) Newtonian flow of heterogeneous synthetic gabbros at high strain: grain sliding, ductile failure, ad contrasting local mechanisms and interactions. European Journal of Mineralogy 23, 303-322.

Goldsby, D. L., and Kohlstedt, D. L. (2001) Superplastic deformation of ice: experimental observations. Journal of Geophysical Research, 106 (B6), 11017–11030.

Guignard, J., Bystricky, M., and Béjina, F. (2011) Dense fine-grained aggregates prepared by spark plasma sintering (SPS), an original technique in experimental petrology. European Journal of Mineralogy 23, 323-331.

Hansen, L.N., Zimmerman, M.E., and Kohlstedt, D.L. (2011) Grain boundary sliding in San Carlos olivine: Flow law parameters and crystallographic-preferred orientation. Journal of Geophysical Research 116, B08201.

Hansen, L.N., Zimmerman, M.E., and Kohlstedt, D.L. (2012a) Laboratory measurements of the viscous anisotropy of olivine aggregates. Nature. 2012 492 (7429):415-8.

Hansen, L.N., Zimmerman, M.E., and Kohlstedt, D.L. (2012b) The influence of microstructure on deformation of olivine in the grain-boundary sliding regime. Journal of Geophysical Research 117, B09201.

Hirth, G., and Kohlstedt, D.L. (1995a) Experimental constraints on the dynamics of the partially molten upper mantle: 1. Deformation in the diffusion creep regime. Journal of Geophysical Research 100, B2, 1981-2001.

Hirth, G., and Kohlstedt, D.L. (1995b) Experimental constraints on the dynamics of the partially molten upper mantle: 2. Deformation in the dislocation creep regime. Journal of Geophysical Research 100, 15441-15449.

Hirth, G., and Kohlstedt, D.L. (2003) Rheology of the upper mantle and the mantle wedge: a view from the experimentalists. In J. Eiler, Ed., Inside the Subduction Factory, 83-115. Geophysical Monograph Series, American Geophysical Union, Washington, DC.

Jackson, I., Faul, U.H., and Skelton, R. (2013) Elastically Accommodated Grain-boundary Sliding: New Insights from Experiment and Modeling. Physics of the Earth and Planetary Interiors 1-32.

Jung, H., Katayama, I., Jiang, Z., Hiraga, T., and Karato, S. (2006) Effect of water and stress on the lattice preferred orientation of olivine. Tectonophysics 421 (1-2), 1-22.

Kumamoto, K.M., Thom, C.A., Wallis, D., Hansen, L.N., Armstrong, D.E.J., Warren, J.M., Goldsby, D.L., and Wilkinson, A.J. (2017) Size effects resolve discrepancies in 40 years of work on low-temperature plasticity in olivine. Science Advances, 3-9.

Karato, S. (2008) Deformation of Earth Materials: an Introduction to the Rheology of Solid Earth. Cambridge University press, Cambridge, UK.

Karato, S., and P. Wu, P. (1993) Rheology of the upper mantle: A synthesis. Science 260, 771–778.

Karato, S., Paterson, M.S., and FitzGerald, J.D. (1986) Rheology of synthetic olivine aggregates: Influence of grain size and water. Journal of Geophysical Research, 91, 8151–8176.

Kohlstedt, D.L., and Goetze, C. (1974) Low-stress high-temperature creep in olivine single crystals. Journal of Geophysical Research, 79, 2045–2051.

Kohlstedt, D.L., and Wang, Z. (2001) American Geophysical Union Fall Meeting, T21C-01.

Mackwell, S. J. (1991) High-temperature rheology of enstatite: Implications for creep in the mantle. Geophysical Research Letters, 18, 2027-2030.

Mainprice and P.G. Silver, P.G. (1993) Interpretation of SKS-waves using samples from the subcontinental lithosphere. Physics of the Earth and Planetary Interiors 78, 257–280.

Mainprice, D., Barruol, G., and Ben Ismaïl, W. (2000) The anisotropy of the Earth's mantle: From single crystal to polycrystal. In S. Karato, A.M. Forte, R.C. Liebermann, G. Masters and L. Stixrude, Eds., Mineral Physics and Seismic Tomography: From Atomic to Global, 117, pp. 237-264. Geophysical Monograph Series, American Geophysical Union, Washington, DC.

Mainprice, D., Tommasi, A., Couvy, H., Cordier, P., and Frost, D.J. (2005) Pressure sensitivity of olivine slip systems and seismic anisotropy of Earth's upper mantle. Nature 433, 731–733.

Manthilake, M. A.G.M., Walter, N., and Frost, D.J. (2012) A new multi-anvil press employing six independently acting 8 MN hydraulic rams. High Pressure Research, 32-2, 195-207.

Marquardt, K., Rohrer, G.S., Morales, L., Rybacki, E., Marquardt, H., and Lin, B. (2015) The most frequent interfaces in olivine aggregates: the GBCD and its importance for grain boundary related processes. Contribution to Mineralogy and Petrology 170:40.

Marquardt, K., De Graef, M., Singh, S., Marquardt, H., Rosenthal, A., and Koizuimi, S. (2017) Quantitative electron backscatter diffraction (EBSD) data analyses using the dictionary indexing (DI) approach: Overcoming indexing difficulties on geological materials. American Mineralogist, 102, 1843–1855.

Maruyama, G., and Hiraga, T. (2017a) Grain- to multiple-grain-scale deformation processes during diffusion creep of forsterite + diopside aggregate: 1. Direct observations. Journal of Geophysical Research, 122, 5890-5915.

Maruyama, G., and Hiraga, T. (2017b) Grain- to multiple-grain-scale deformation processes during diffusion creep of forsterite + diopside aggregate: 2. Grain boundary sliding-induced grain rotation and its role in crystallographic preferred orientation in rocks. Journal of Geophysical Research, 122, 5916–5934.

Miyazaki, T., Sueyoshi, K., and Hiraga, T. (2013) Olivine crystals align during diffusion creep of Earth's upper mantle. Nature, 502, 321-326.

Molodov, D.A., Gorkaya, T., and Gottstein, G. (2011a) Dynamics of grain boundaries under applied mechanical stress. Journal of Materials Science, 46, 4318-4326.

Molodov, D.A., Gorkaya, T., and Gottstein, G. (2011b) Migration of Σ7 tilt grain boundary in Al under an applied external stress. Scripta Materialia, 65, 990-993.

Montagner, J.P., and Tamimoto, T. (1991) Global upper mantle tomography of seismic velocities and anisotropies. Journal of Geophysical Research: Solid Earth banner, 96 (B12), 20337-20351.

Nicolas, A., and Poirier, J.P. (1976) Crystalline Plasticity and Solid State Flow in Metamorphic Rocks,444 pp., John Wiley, London, UK.

Nicolas, A., and Christensen, N.I. (1987) Formation of anisotropy in upper mantle peridotites - a review, in: K. Fuchs, C. Froidevaux (Eds.), Composition, Structure and Dynamics of the Lithosphere–Asthenosphere System, 16, 111-123. American Geophysical Union, Washington, DC.

Nicolas, A., Boudier, F., and Boullier, A.M. (1973) Mechanism of flow in naturally and experimentally deformed peridotites. American Journal of Sciences 273, 853–876.

Ohuchi, T., Kawazoe, T., Higo, Y., Funakoshi, K.I., Suzuki, A., Kikegawa, T., and Irifune, T. (2015) Dislocation-accommodated grain boundary sliding as the major deformation mechanism of olivine in the Earth's upper mantle. Science Advances, vol.1, 9, e1500360.

Peach, C.J., and Spiers, C.J. (1996) Influence of crystal plastic deformation on dilantacy and permeability development in synthetic salt rock. Tectonophysics, 256, 101–128.

Poirier, J.P. (1985) Creep of crystals, High temperature deformation processes in metals, ceramics and minerals. Cambridge Earth Science Series, Cambridge University press, Cambridge, UK.

Quintanilla-Terminel, A., and Evans, B. (2016) Heterogeneity of inelastic strain during creep of Carrara marble: Microscale strain measurement technique. Journal of Geophysical Research, Solid Earth, 121, 5736–5760.

Quintanilla-Terminel, A., Zimmerman, M., Evans, B., and Kohlstedt, D. (2017) Microscale and nanoscale strain mapping techniques applied to creep of rocks. Solid Earth 8 (4), 751.

Raleigh, C.B. (1965) Glide mechanisms in experimentally deformed minerals. Science, 150 (3697), 739–741.

Raterron, P., Detrez, F., Castelnau, O., Bollinger, C., Cordier, P., and Merkel, S. (2014) Multiscale modeling of upper mantle plasticity: From single-crystal rheology to multiphase aggregate deformation. Physics of the Earth and Planetary Interiors, 228, 232-243.

Rollett, A.D., Wagner, F., Allain-Bonasso, N., Field, D.P., and Lebensohn, R.A. (2012) Comparison of Gradients in Orientation and Stress between Experiment and Simulation. Materials Science Forum, 702, 463–468.

Tasaka, M., Hiraga, T., and Zimmerman, M.E. (2013) Influence of mineral fraction on the rheological properties of forsterite + enstatite during grain-size-sensitive creep: 2. Deformation experiments. Journal of Geophysical Research, Solid Earth, 118, 3991-4012.

Tasaka, M., Zimmerman, M.E., and Kohlstedt, D.L. (2016) Evolution of the rheological and microstructural properties of olivine aggregates during dislocation creep under hydrous conditions. Journal of Geophysical Research, Solid Earth, 121-1, 92-113.

Ter Heege, J.H., De Bresser, J.H.P., and Spiers, C.J. (2004) Composite flow laws for crystalline materials with log-normally distributed grain size: theory and application to olivine. Journal of Structural Geology 26 (9), 1693- 1705.

Tielke, J.A., Hansen, L.N., Tasaka, M., Meyers, C., Zimmerman, M.E., and Kohlstedt, D.L. (2016) Observations of grain size sensitive power law creep of olivine aggregates over a large range of lattice-preferred orientation strength. Journal of Geophysical Research 121, 506-516.

Tommasi, A., Mainprice, D., Canova, G. R., and Chastel, Y. (2000) Viscoplastic self-consistent and equilibrium-based modeling of olivine lattice preferred orientations: Implications for the upper mantle seismic anisotropy. Journal of Geophysical Research 105, 7893-7908.

Warren, J.M., and Hirth, G. (2006) Grain size sensitive deformation mechanisms in naturally deformed peridotites. Earth and Planetary Science Letters 248, 438-450.

Warren, J.M., Hirth, G., and Kelemen, P.B. (2008) Evolution of olivine lattice preferred orientation during simple shear in the mantle. Earth and Planetary Science Letters 272, 501-512.

Wright, S.I, Nowell, M.M., and Field, D.P. (2011) A Review of Strain Analysis Using Electron Backscatter Diffraction. Microscopy and Microanalysis, 17(3), 316-329.

Wright, S.I., Nowell, M.M., Scott P. Lindeman, S.P., Camus, P.P., De Graef, M., and Jackson, M.A. (2015) Introduction and comparison of new EBSD post-processing methodologies. Ultramicroscopy, 159-1, 81-94.

Xu, L., and Evans, B. (2010) Strain heterogeneity in deformed Carrara marble using a microscale strain mapping technique. Journal of Geophysical Research 115, B04202.

Weertman, J., and Weertman, J.R. (1975) High temperature creep of rock and mantle viscosity. Annual Reviews of Earth and Planetary Sciences, 3, 293–315.

Zhao, Y. H., Li, X.F., Zimmerman, M., and Kohlstedt, D.L. (2009) Simple shear deformation experiment on iron rich olivine aggregates. Acta Petrolei Sinica 25 (10), 2687-2693.

TABLES CAPTIONS

Table 1: details of the experimental conditions.

Table 2: details of the KAM distribution in all samples.

FIGURES CAPTIONS

Fig. 1: Split cylinder setup and grid-geometry.

(a) Schematic of the split cylinder with the grid on one face.

(b) Procedure to protect the sample (green) from Gallium (blue) deposition during the milling (see text for details) before the EBSD mapping with a PMMA layer (yellow).

(c) Final split-cylinder with a thin slice of NaCl between both halves. The red arrows show the direction of the compression.

Fig. 2: Experimental procedure overview (a) SE picture of the sample M611 (3.5 GPa; 1000 °C; $\dot{\varepsilon} = 2.0x10^{-5}s^{-1}$; ε_p=15%) after milling the grid (appearing in white). The black frame represents the part of the sample recovered after the experiment, as shown in SE in (b) and (d). The black regions cover a crack (b) excluded from EBSD analyses. (c) Inverse pole map (color code inserted, Pnma) of the grains of the recovered surfaces before and after (d) the deformation. The compression direction is horizontal.

Fig. 3: In-plane grain boundary motion (strain marker offsets indicated with black arrows) before (BSE) and after deformation (SE):

a, b, c) M585 (5.5 GPa; 1050 °C; $\dot{\varepsilon} = 1.1x10^{-5}s^{-1}$; ε_p=17%). The white arrow shows the curvature of the grid.

d, e) M582 (5.0 GPa; 1000 °C; $\dot{\varepsilon} = 2.0x10^{-5}s^{-1}$; ε_p=30%).

f, g) M615 (3.5 GPa, 1200 °C, $\dot{\varepsilon} = 2.0x10^{-5}s^{-1}$; ε_p=15%) after deformation. White arrow show a grain that slightly popped up. The white circle shows a grain that slightly rotated counterclockwise as indicated by the offset close to the black arrow. The gray arrow in f) shows a bend of the strain marker. The compression direction is horizontal. See text for more details.

Fig. 4: Out-of-plane grain boundary motion. (a) sample M640 (5.0 GPa; 1000 °C; $\dot{\varepsilon} = 2.0x10^{-5}s^{-1}$; ε_p=40%). (b) sample M639 (5.0 GPa; 1200 °C; $\dot{\varepsilon} = 2.0x10^{-5}s^{-1}$; ε_p=40%). The compression direction is horizontal. 1) grain pushed away from the camera; 2) grain pushed toward from the camera; 3) surface tilting.

Fig. 5: the KAM (a-b) and GROD (c-d) from the same region before and after the deformation of the sample M640 (5.0 GPa; 1050 °C; $\dot{\varepsilon} = 2.0x10^{-5}s^{-1}$; ε_p=40%).We can clearly observe the higher intragranular plasticity after the deformation with the KAM (5°), and the strain that developed in the grains with the GROD (20°). Those tools highlight in the grain the high dislocation density at some subgrains boundaries (black arrow). Color scale bars in degrees with max. value: the most disoriented pixel; min. value: the less disoriented pixel. We highlighted some grain boundaries in white as a guide to the eyes.

Fig. 6: a, b) two GROD (20°) maps for sample M585 (5.5 GPa; 1050 °C; $\dot{\varepsilon} = 1.1x10^{-5}s^{-1}$; ε_p=17%); c) GROD (20°) for M576 (5.0 GPa; 1100 °C; $\dot{\varepsilon} = 2.0x10^{-5}s^{-1}$); ε_p=28%); d) GROD (20°) for M611 (3.5 GPa; 1000 °C; $\dot{\varepsilon} = 2.0x10^{-5}s^{-1}$; ε_p=15%). Intense GROD is present in some

grains, and localized near some grain boundaries and triple points. Color scale bars in degrees with max. value: the most disoriented pixel; min. value: the less disoriented pixel.

Fig. 7: GROD maps for the sample M615 (3.5 GPa, 1200 °C, $\dot{\varepsilon} = 2.0x10^{-5}s^{-1}$; ε_p=15%) and M621 (5.0 GPa, 1200 °C, $\dot{\varepsilon} = 2.0x10^{-5}s^{-1}$; ε_p=15%). The GROD (20°) remains still intense at some grain boundaries and triple points than in M585, M576 and M611 (below 1200 °C), even though it is weaker in the grains. There are less heterogeneities from 1100 °C. Color scale bars in degrees with max. value: the most disoriented pixel; min. value: the less disoriented pixel.

Fig. 8: Distribution of the KAM for the sample M621 (5.0 GPa; 1200 °C; $\dot{\varepsilon} = 2.0x10^{-5}s^{-1}$; ε_p=15%). The curve from initial state (dotted lines) is shifted to the right due to the applied strain on the sample, for the bulk (dash line) and the surface (full line).

Fig. 9: a) KAM distribution for all the samples deformed at 5.0 GPa. Deforming at higher temperature leads to a shift on the left of the curves. b) The full width at half maximum FWHM as a function of the temperature. This value is smaller at 1200 °C than at lower temperature.

Fig. 10: KAM plotted versus the grain size (same axis for all the pictures) for M582 and M585 after deformation (and before for M585 as an example) below 1100 °C and M628 deformed at 1200 °C. The color scale (degrees) is the same for all the diagrams, with max. value: the most disoriented pixel; min. value: the less disoriented pixel.

This is a preprint, the final version is subject to change, of the American Mineralogist (MSA)
Cite as Authors (Year) Title. American Mineralogist, in press.
DOI: https://doi.org/10.2138/am-2019-6629

FIGURES CAPTIONS FOR THE SUPPLEMENTARY MATERIALS

Figure A: the 8-mm unfired pyrophyllite cell assembly.

Figure B: M582 (GBiF1-15-8mm) – 5.0 GPa; 1000 °C; $\dot{\varepsilon} = 2.0x10^{-5}s^{-1}$; ε_p=30%.

a) SE picture before deformation showing the grid

b) SE picture after deformation

c) Inverse pole orientation before deformation with the colored insert (*Pnma*) as reference

d) Inverse pole orientation after deformation.

Figure C: M585 (GBiF1-16-8mm) - 5.5 GPa; 1050 °C; $\dot{\varepsilon} = 1.1x10^{-5}s^{-1}$; ε_p=17%

a) SE picture before deformation showing the grid

b) SE picture after deformation

c) Inverse pole orientation before deformation with the colored insert (*Pnma*) as reference

d) Inverse pole orientation after deformation.

Figure D: a) KAM distribution for all the samples deformed at 3.5 GPa. b) The full width at half maximum FWHM as a function of the temperature, in grey for experiments at 3.5 GPa, superposed to experiments at 5.0 GPa in white diamonds.

# Run	P (GPa)	T (°C)	Strain rate $\dot{\varepsilon}$ (10^{-5} s^{-1})	Applied plastic strain ε_p (%)	Grid / marker
M576	5.0	1100	2.0	28	100 µm² and 75 µm² grid
M582	5.0	1000	2.0	30	100 µm² and 75 µm² grid
M585	5.5	1050	1.1	17	100 µm² and 75 µm² grid
M606	3.5	1200	2.0	10	25 µm² grid, partially recovered sample
M611	3.5	1000	2.0	15	25 µm² grid
M615	3.5	1200	2.0	15	25 µm² grid, partially recovered sample
M621	5.0	1200	2.0	15	25 µm² grid, partially recovered sample
M622	5.0	1200	2.0	15	25 µm² grid, partially recovered sample
M628	5.0	1200	2.0	20	25 µm² grid
M639	5.0	1200	2.0	40	25 µm² grid, partially recovered sample
M640	5.0	1000	2.0	40	25 µm² grid

Table 1

# Run	P (GPa)	T (°C)	Strain rate $\dot{\varepsilon}$ (10^{-5} s^{-1})	Applied plastic strain ε_p (%)	Maximum KAM distribution (°)	FWHM
M611	3.5	1000	2.0	15	0.54	0.79
M606	3.5	1200	2.0	10	0.54	0.73
M615	3.5	1200	2.0	15	0.53	0.55
M582	5.0	1000	2.0	30	0.65	0.94
M640	5.0	1000	2.0	40	0.95	1.28
M585	5.5	1050	1.1	17	0.54	0.86
M576	5.0	1100	2.0	28	0.75	0.96
M621	5.0	1200	2.0	15	0.44	0.61
M622	5.0	1200	2.0	15	0.54	0.66
M628	5.0	1200	2.0	20	0.45	0.64
M639	5.0	1200	2.0	40	0.45	0.64

Table 2

Figure 1

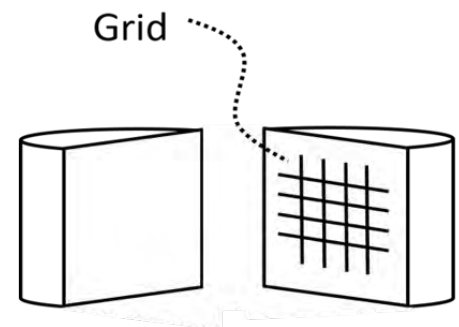

a

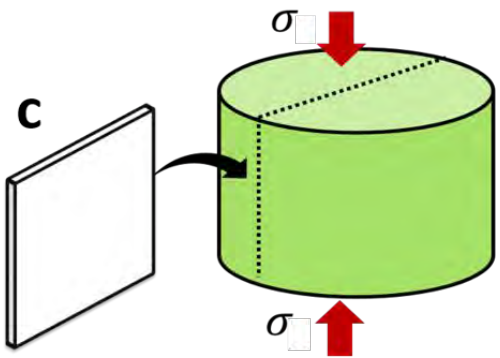

c

NaCl wafer < 150 µm

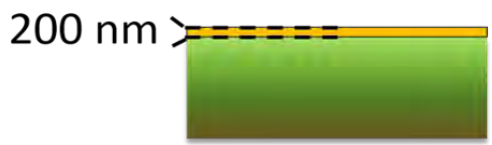

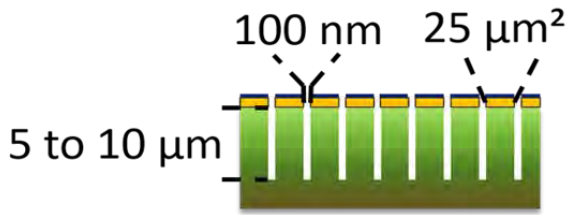

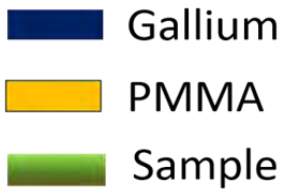

- Acetone 15 min 40°C
- 1/4 diamond polish

b

Figure 2

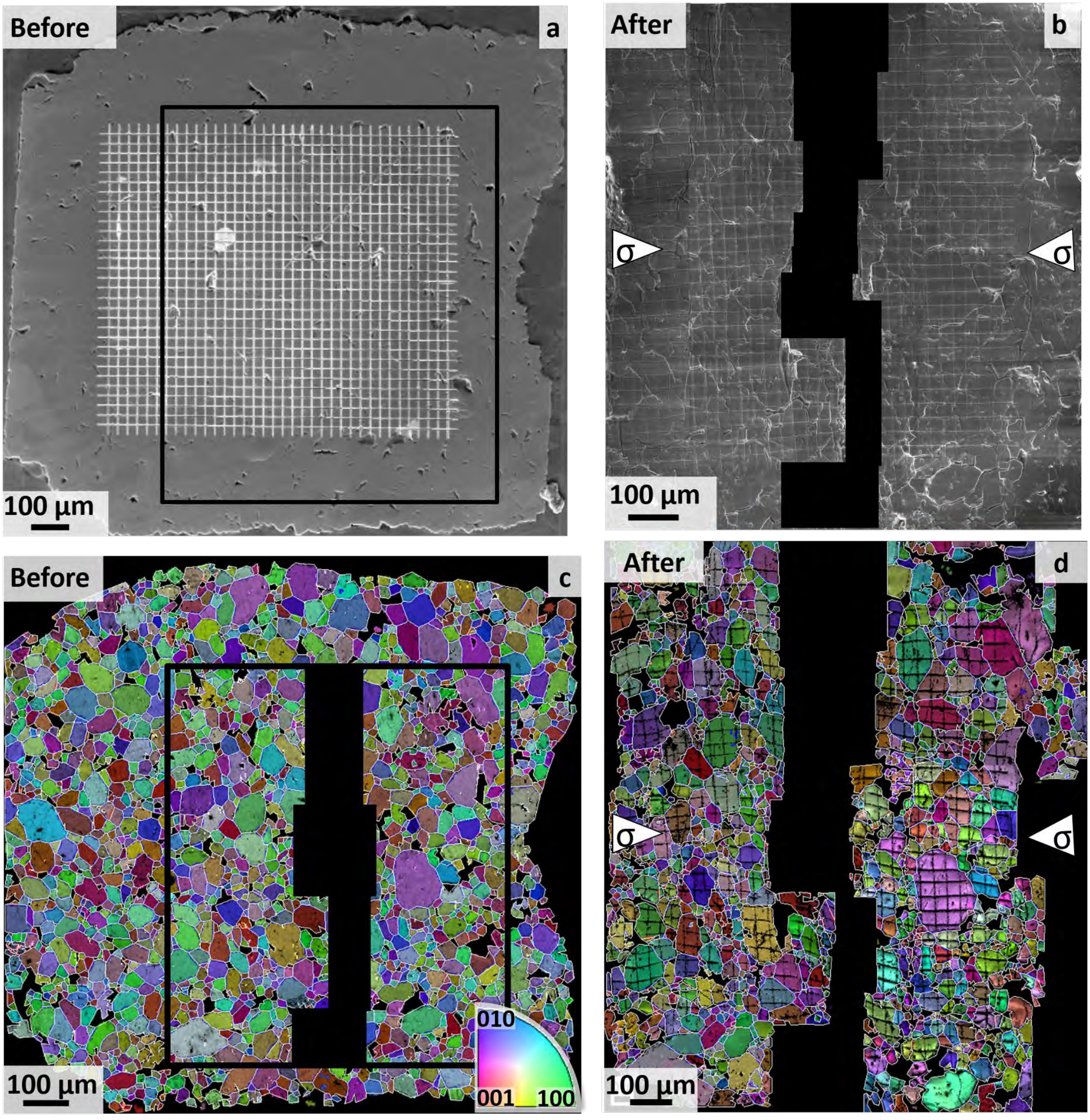
Before
a
100 µm
After
b
σ
σ
100 µm
Before
c
010
001
100
100 µm
After
d
σ
σ
100 µm

Figure 3abc

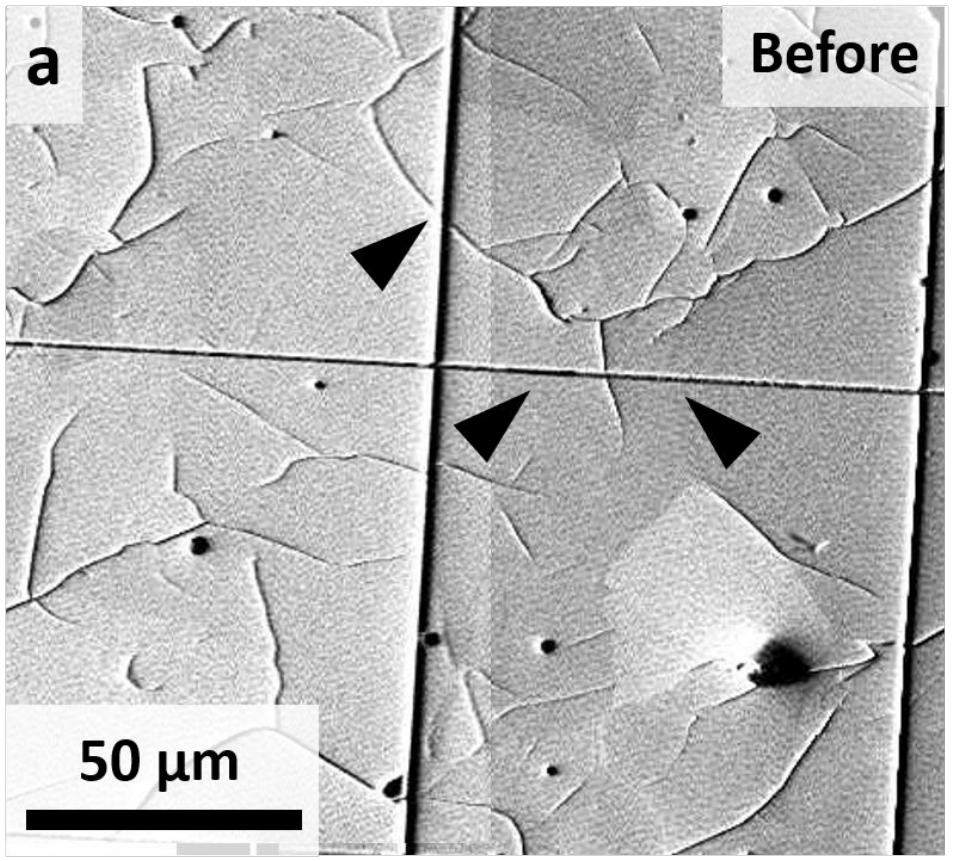

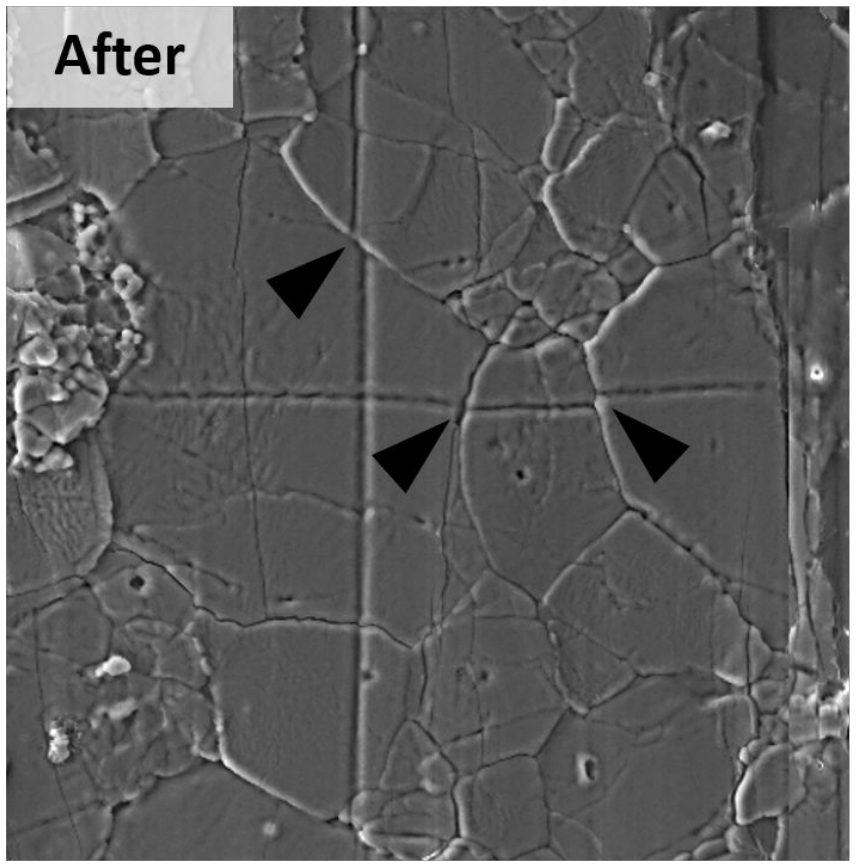

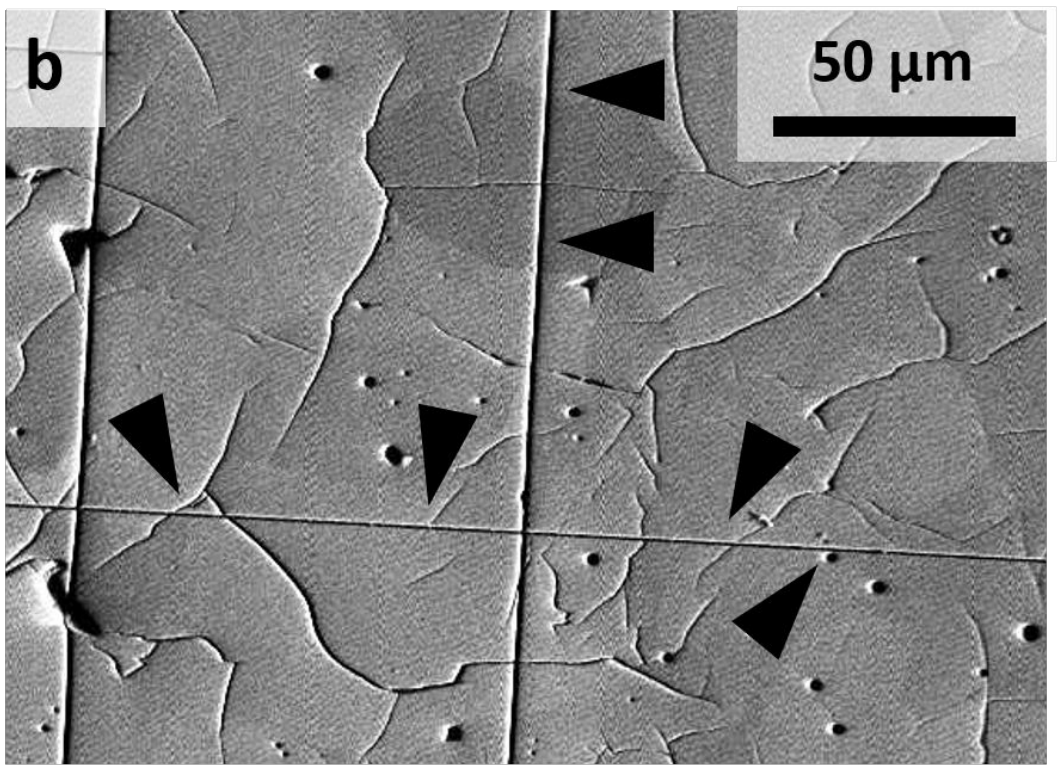

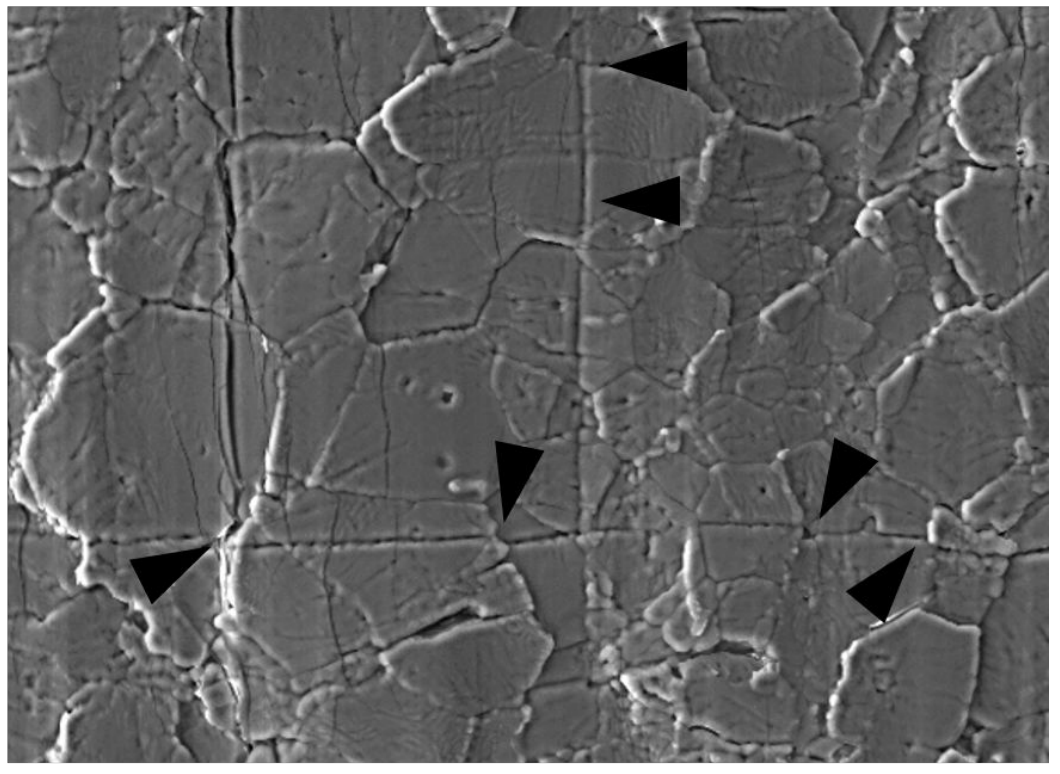

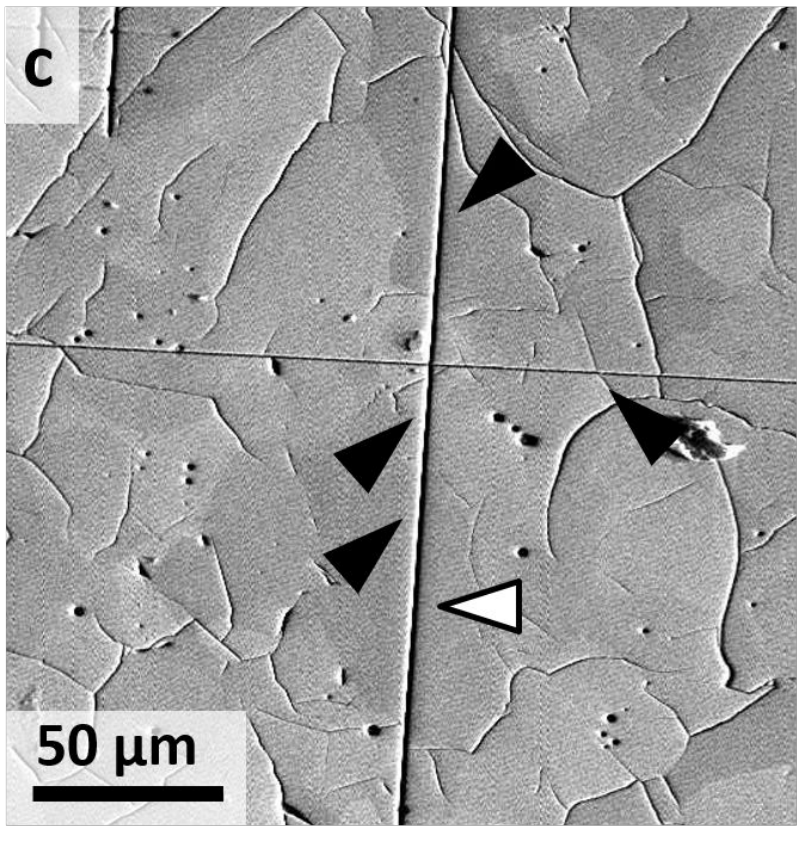

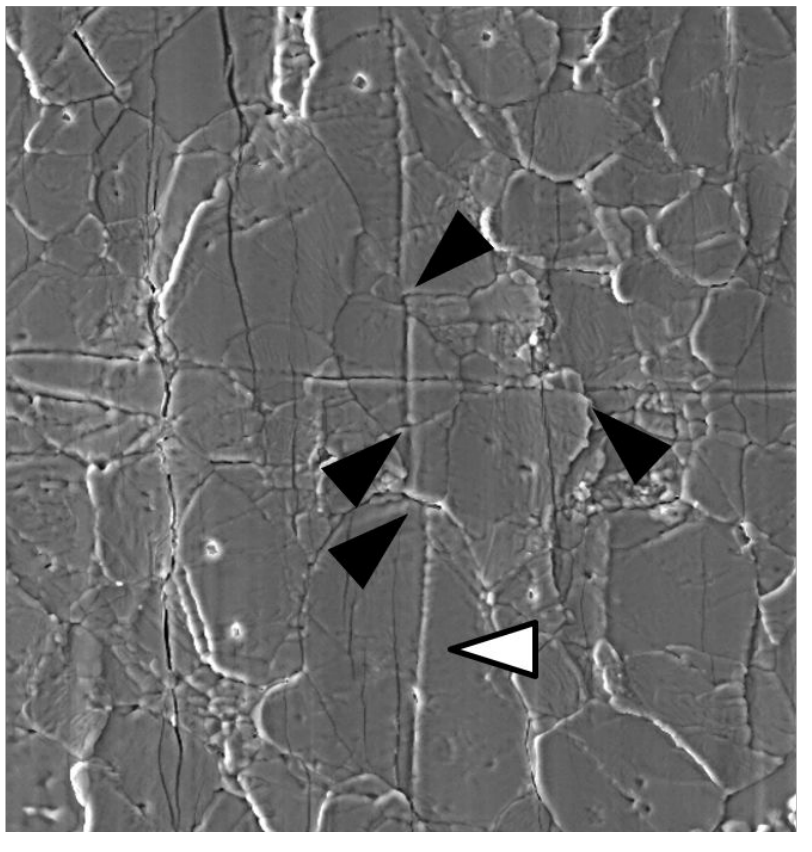

Figure 3defg

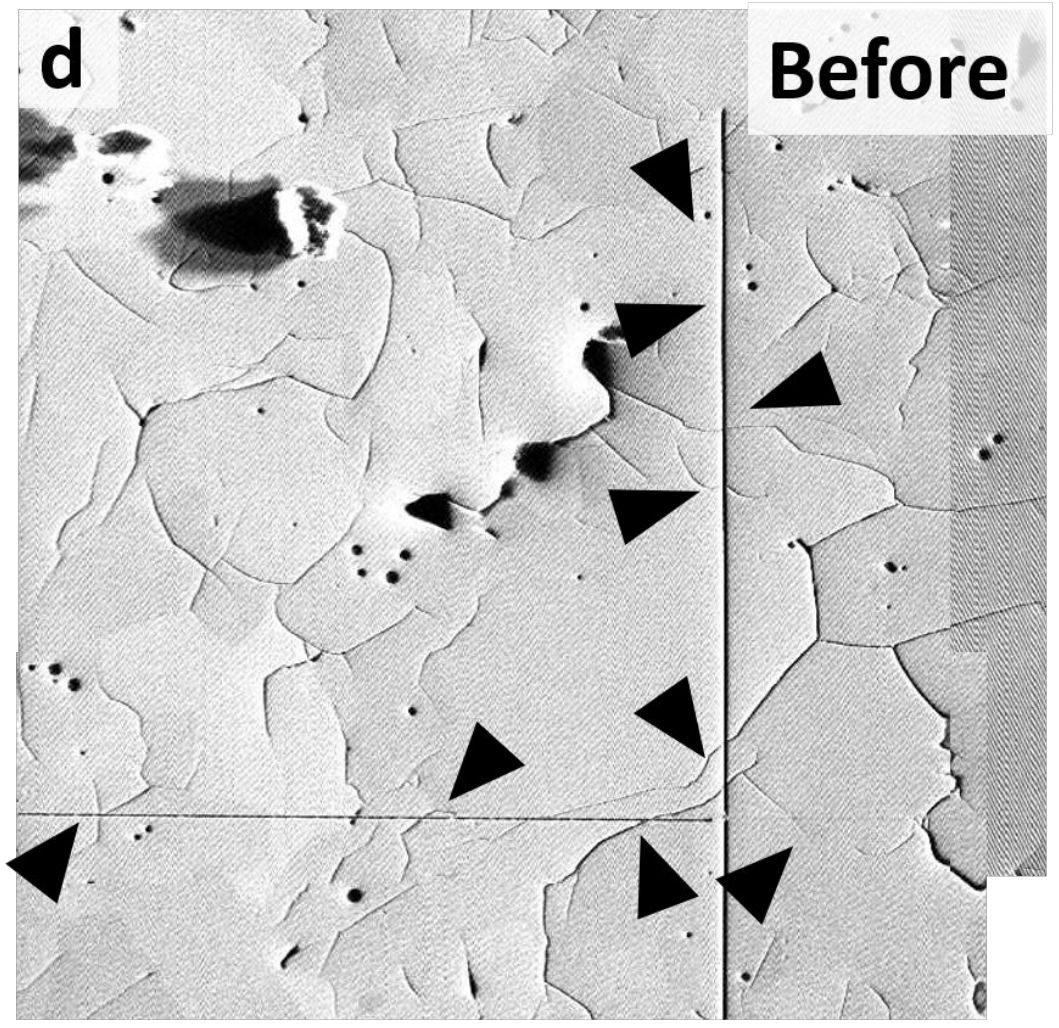

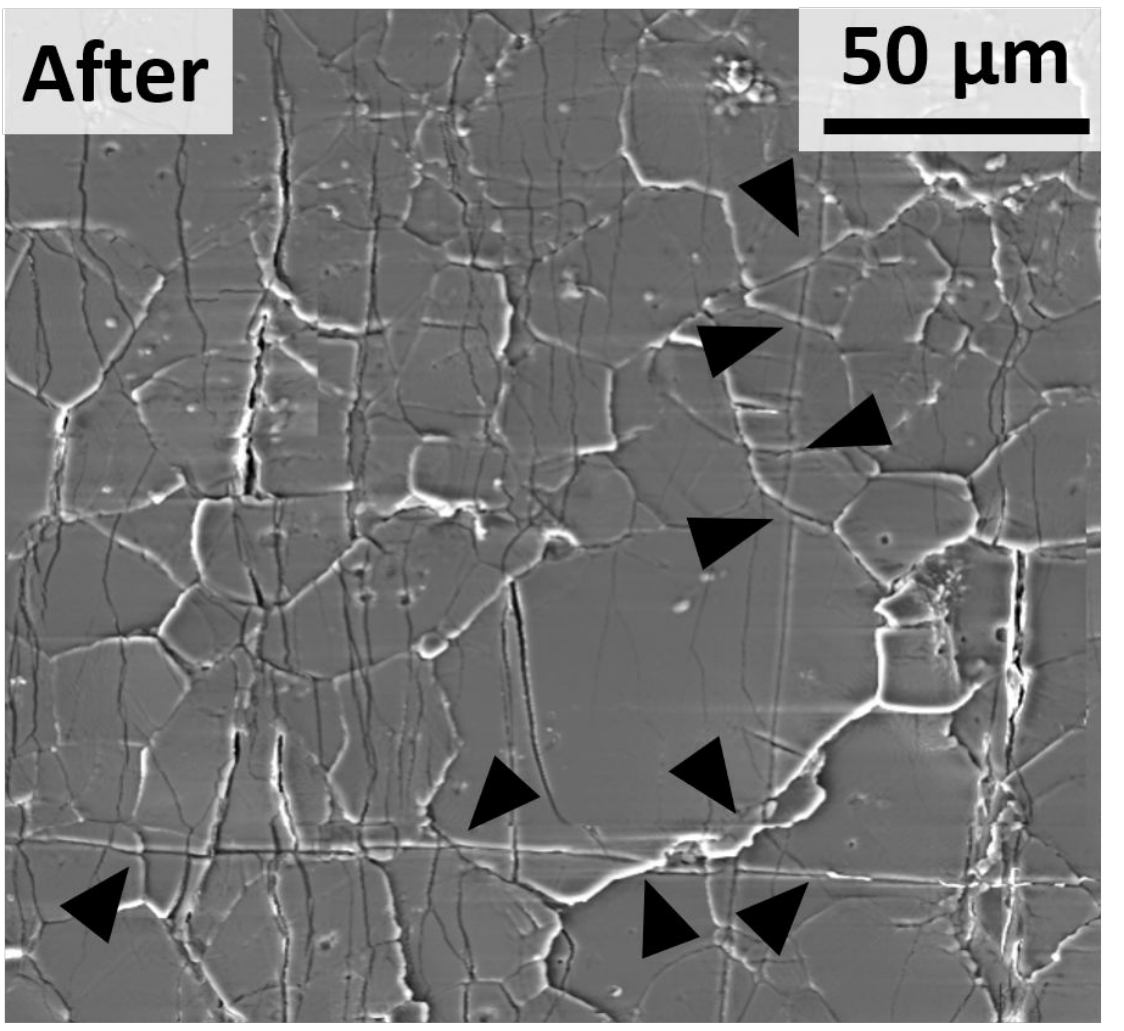

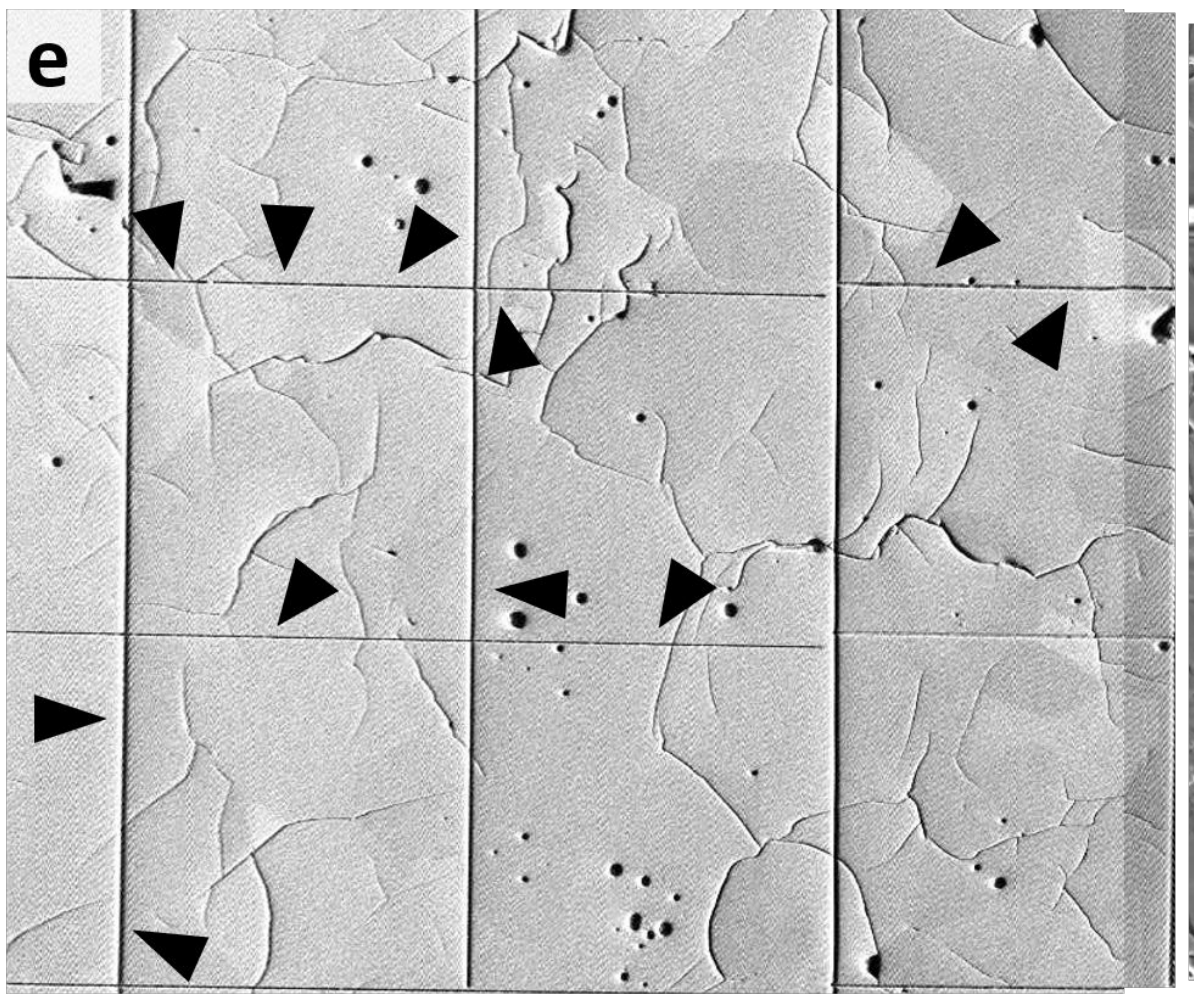

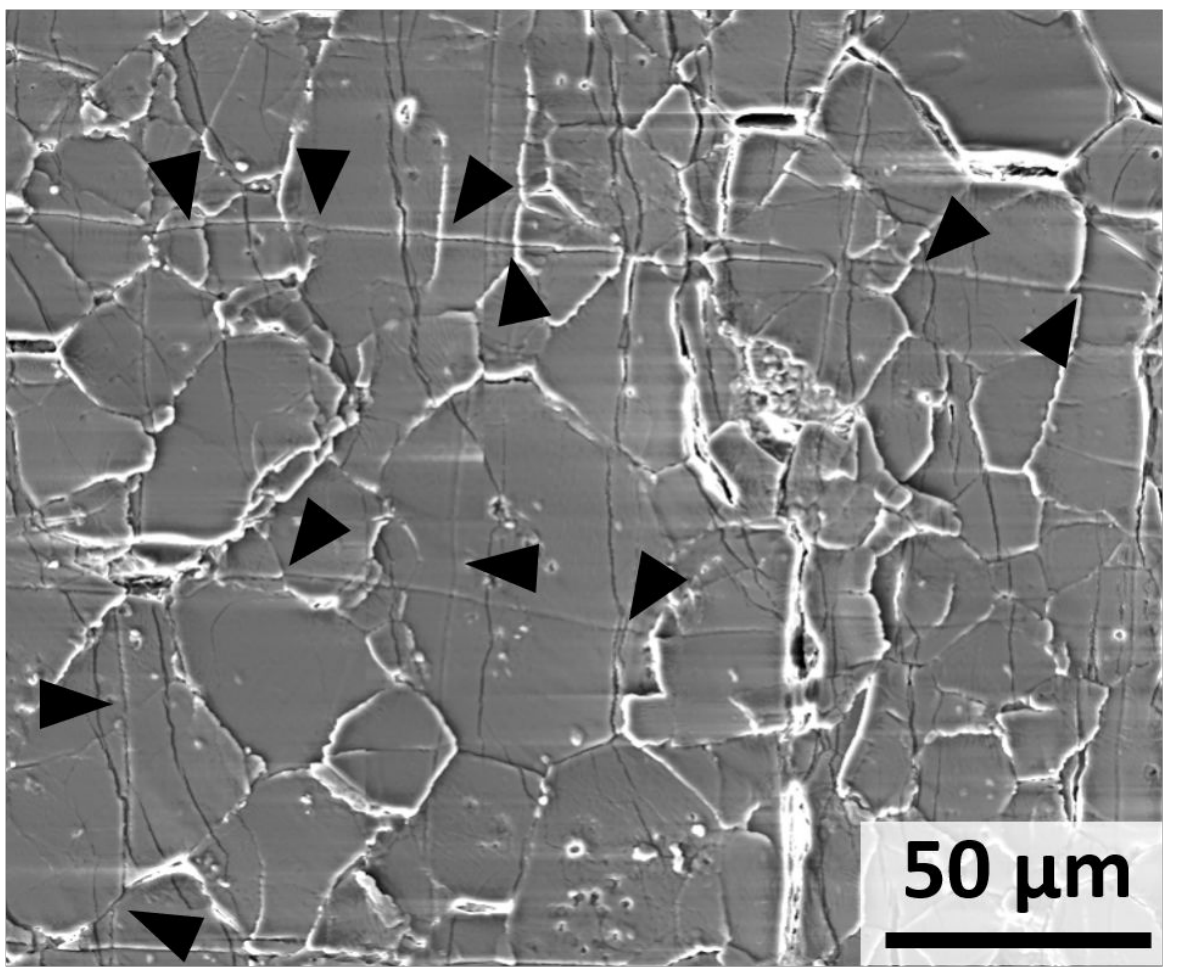

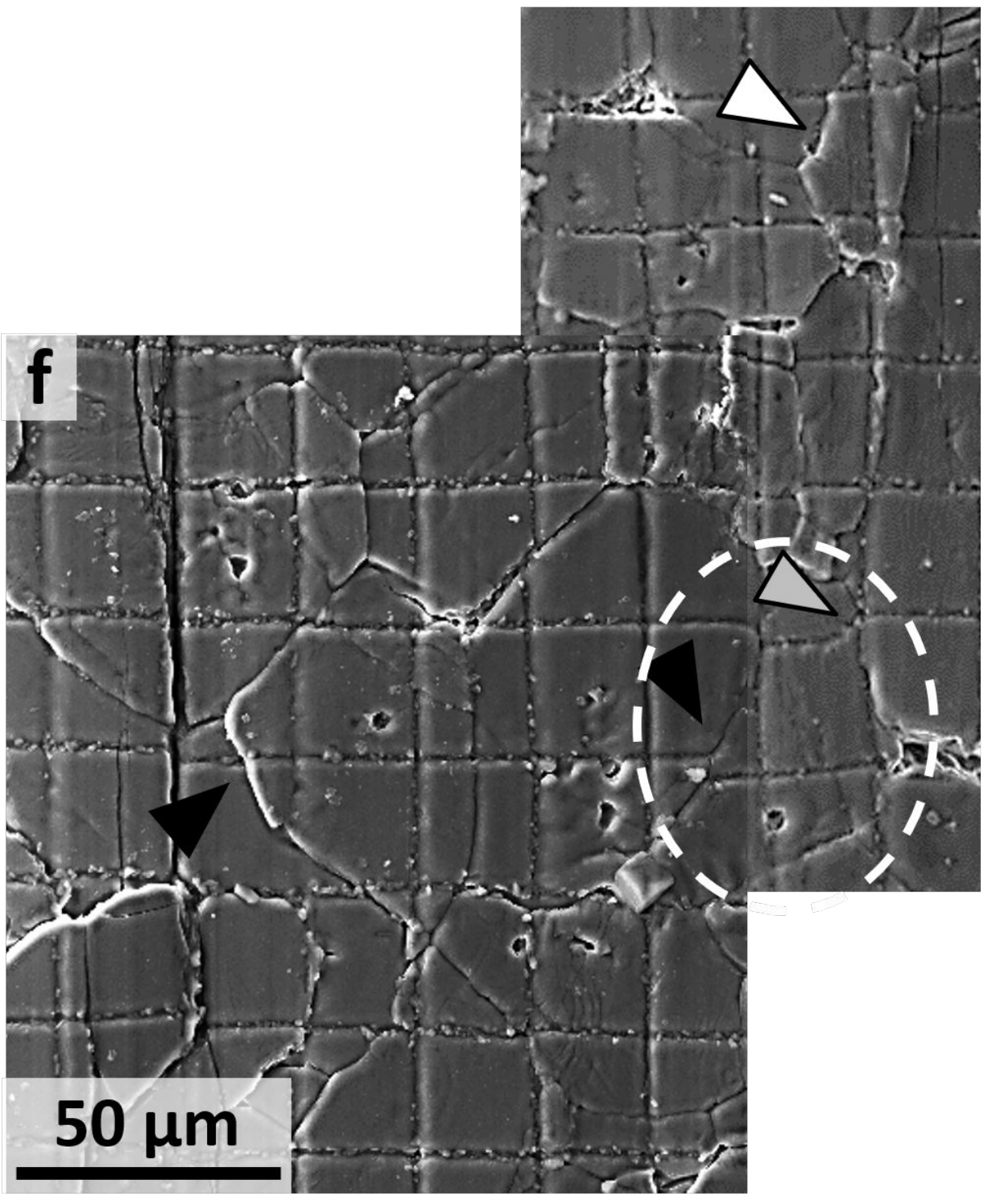

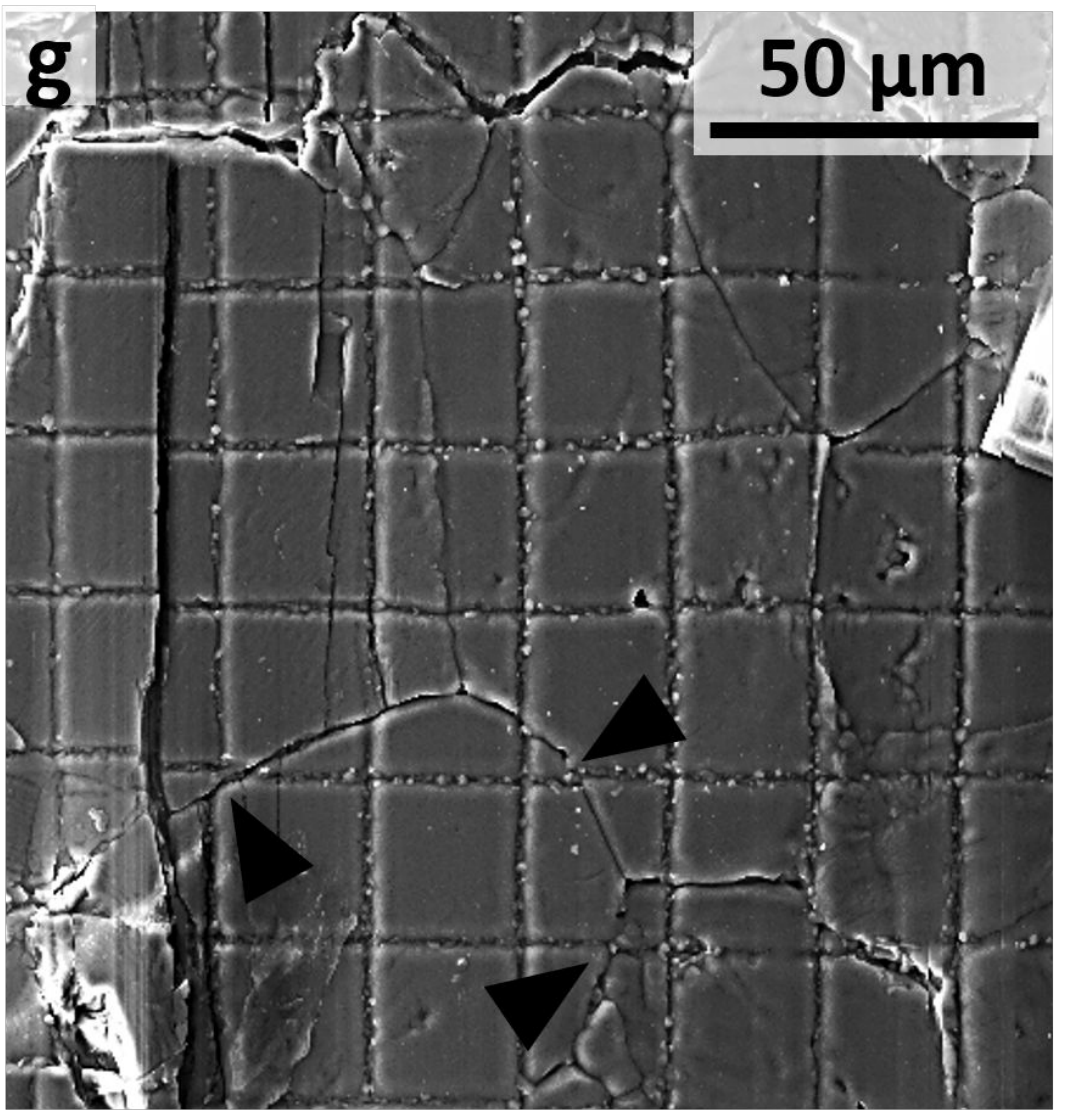

Figure 4

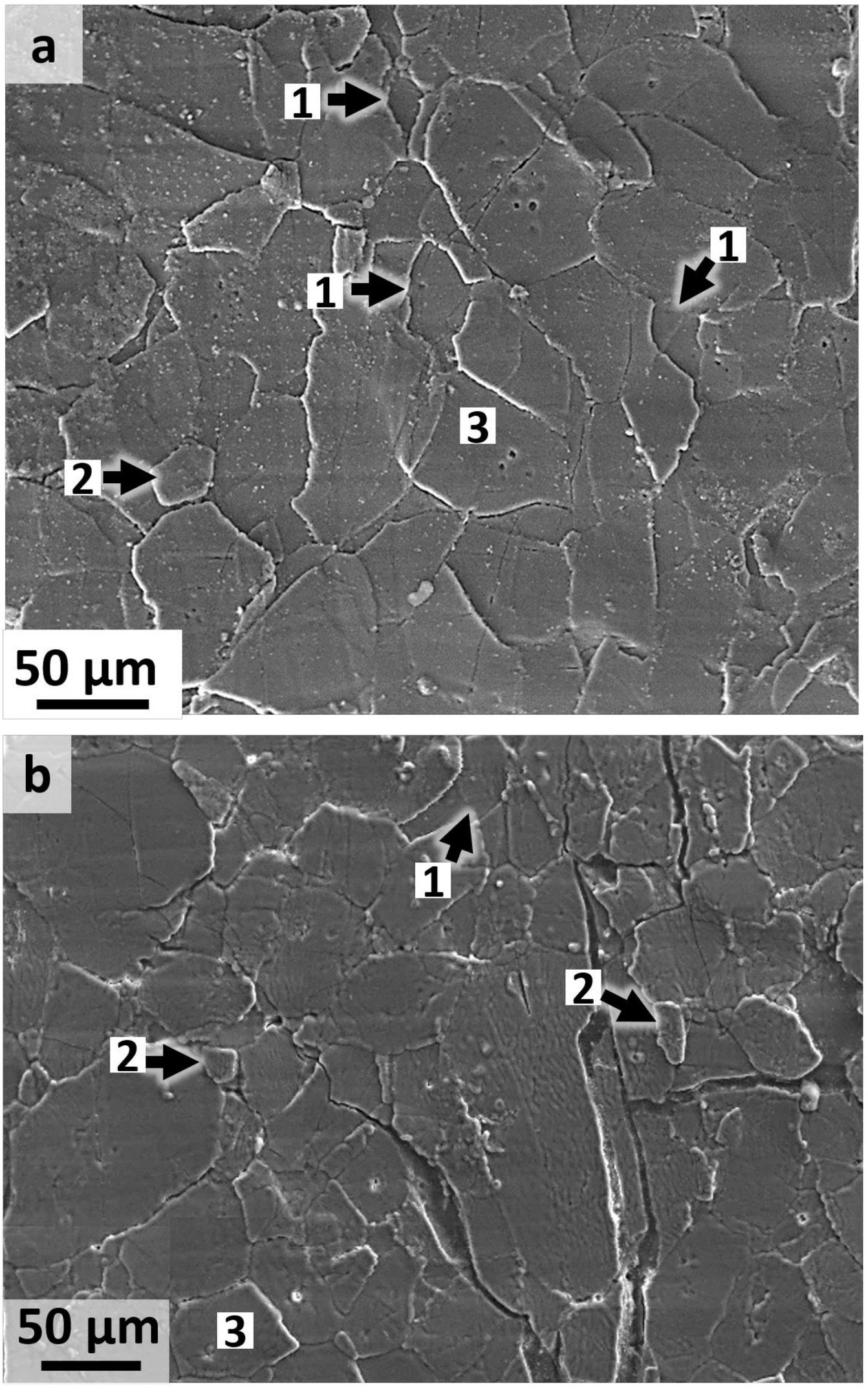

Figure 5

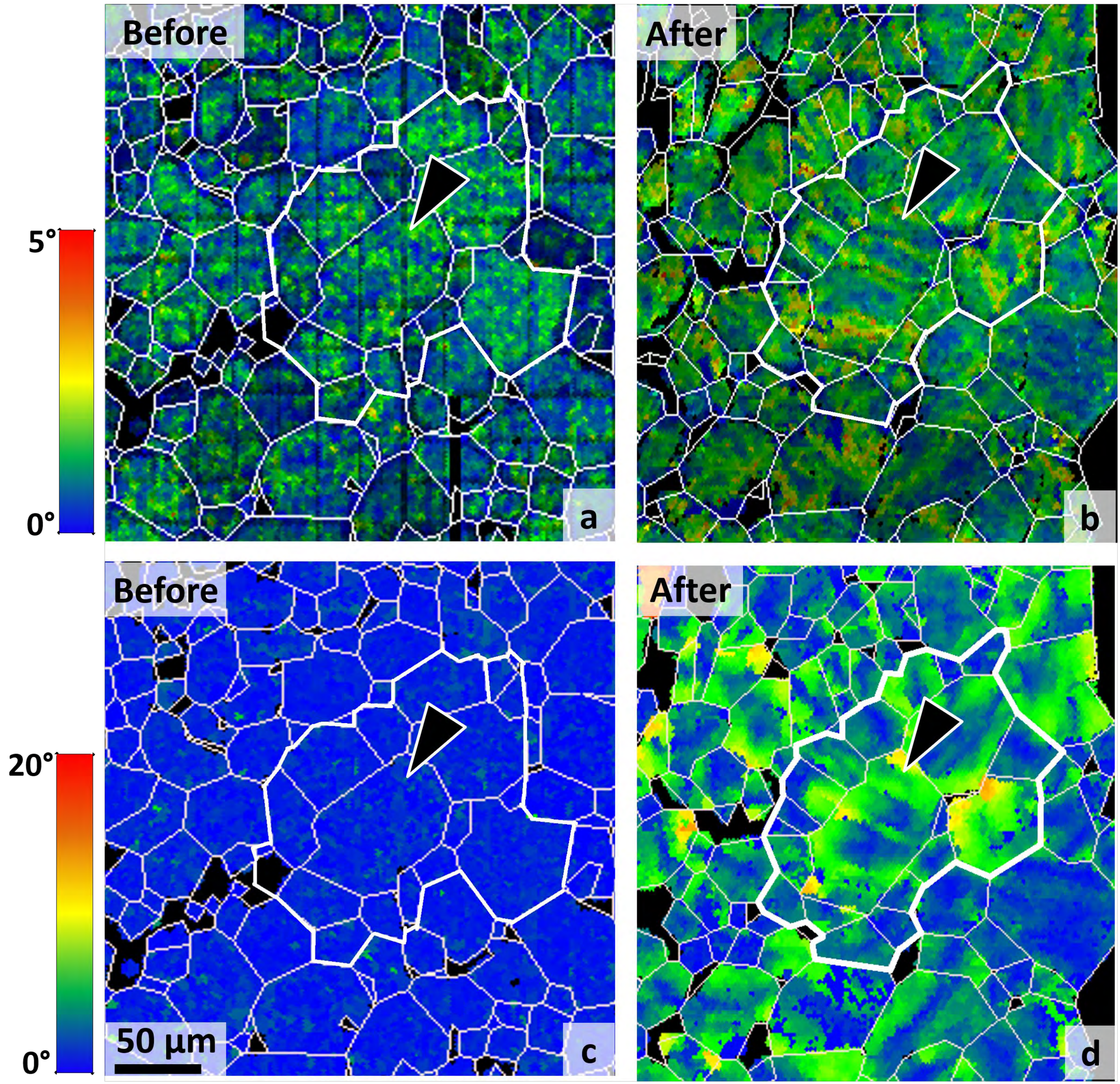

Figure 6

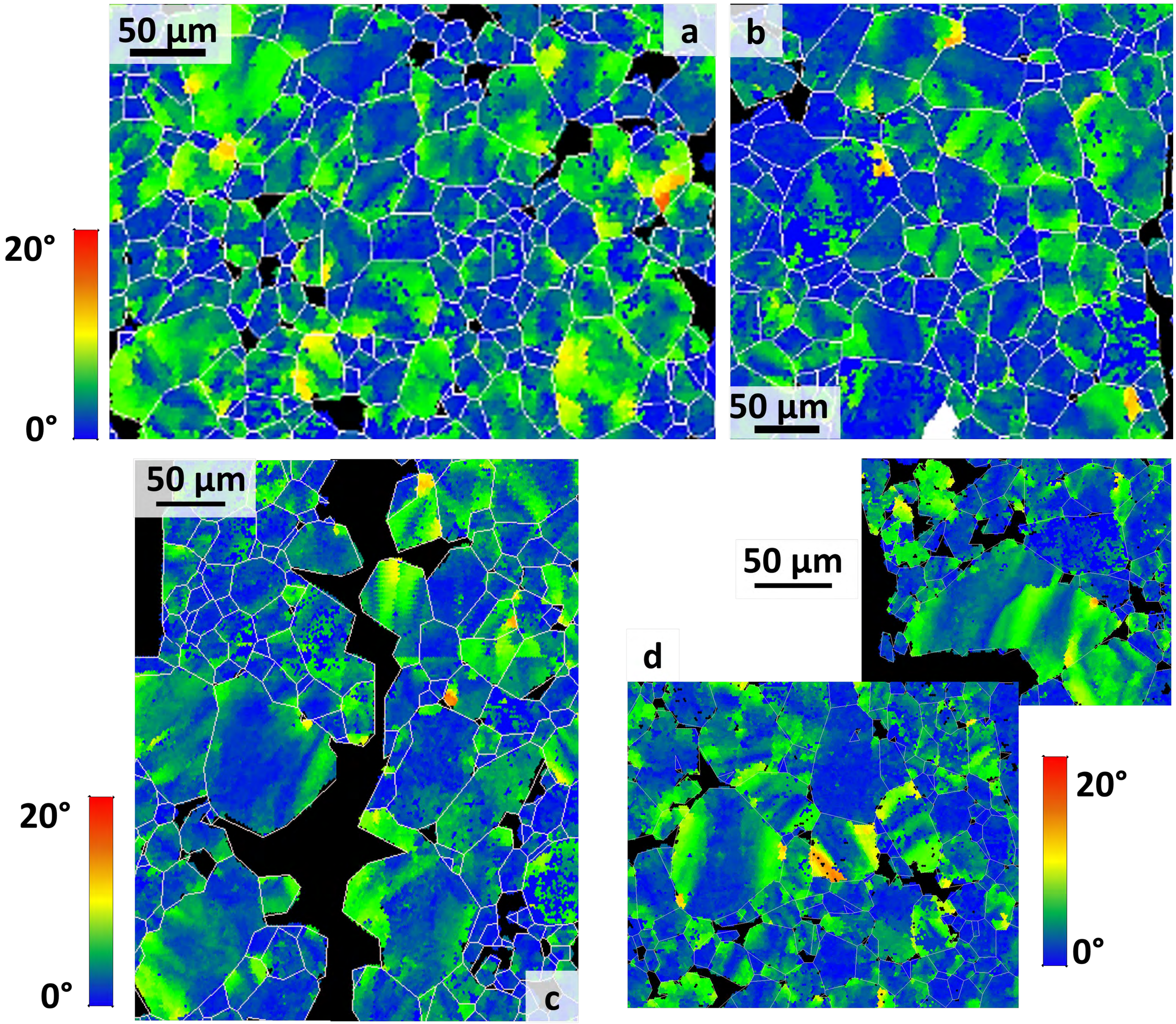

Figure 7

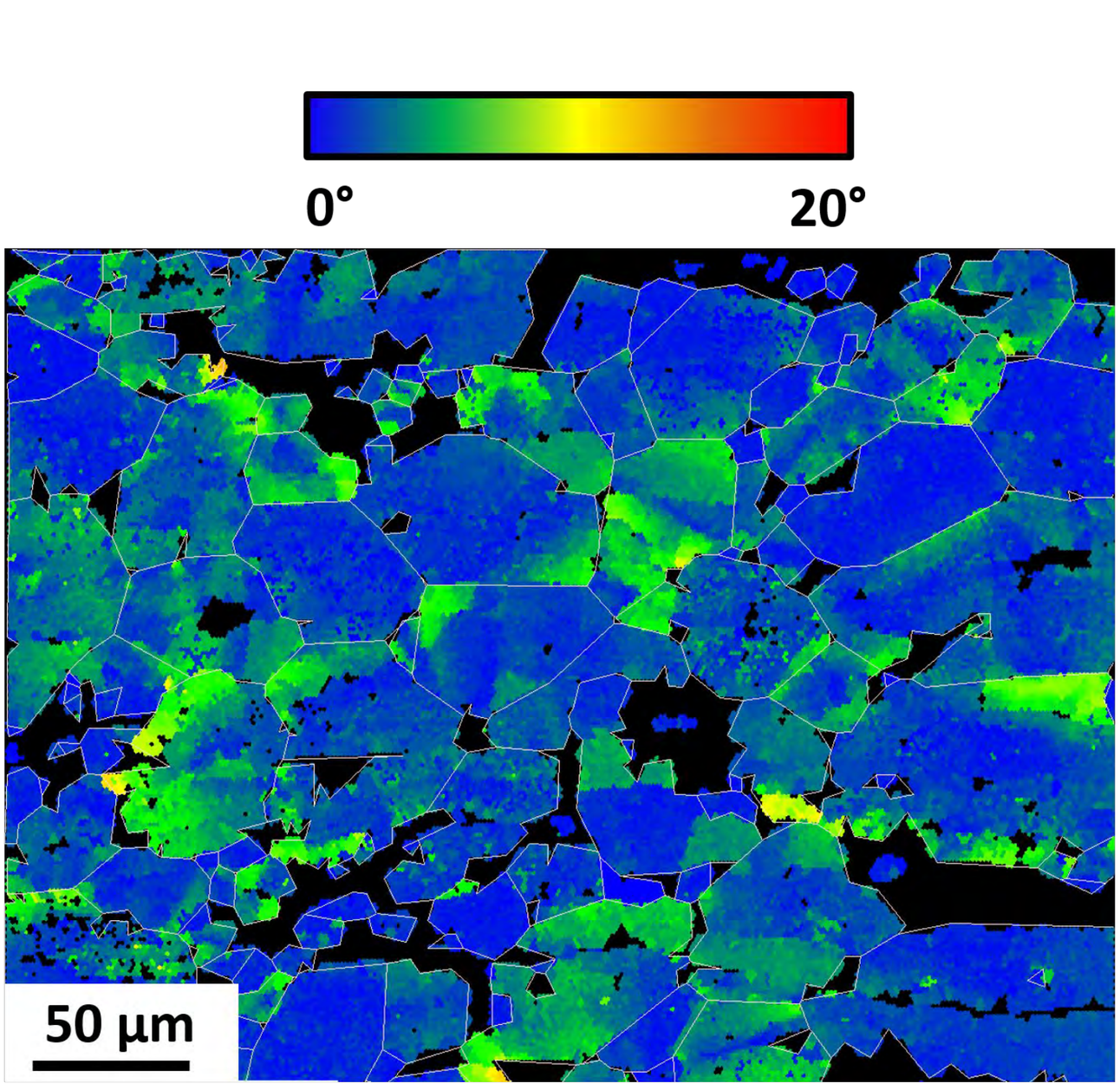

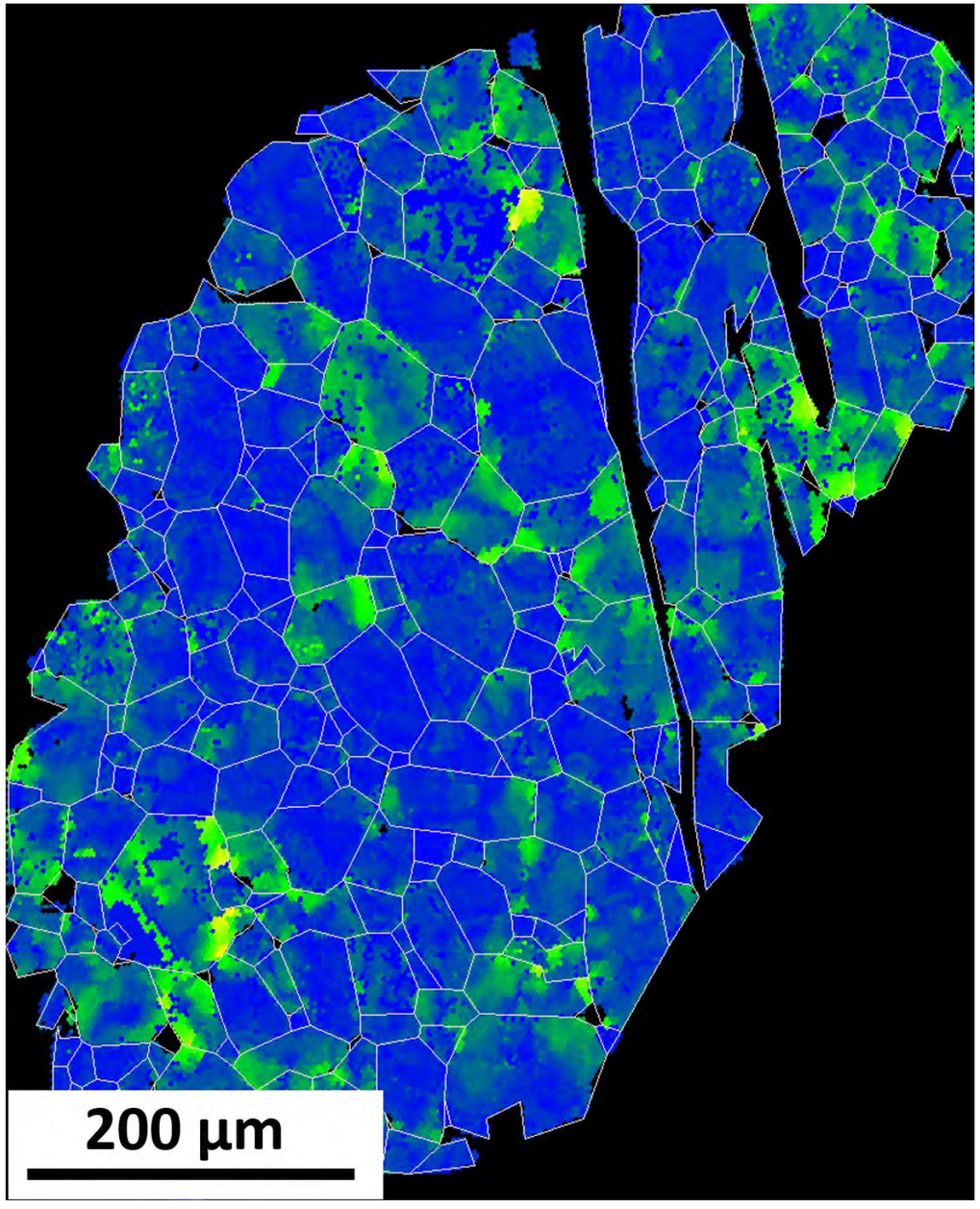

Figure 8

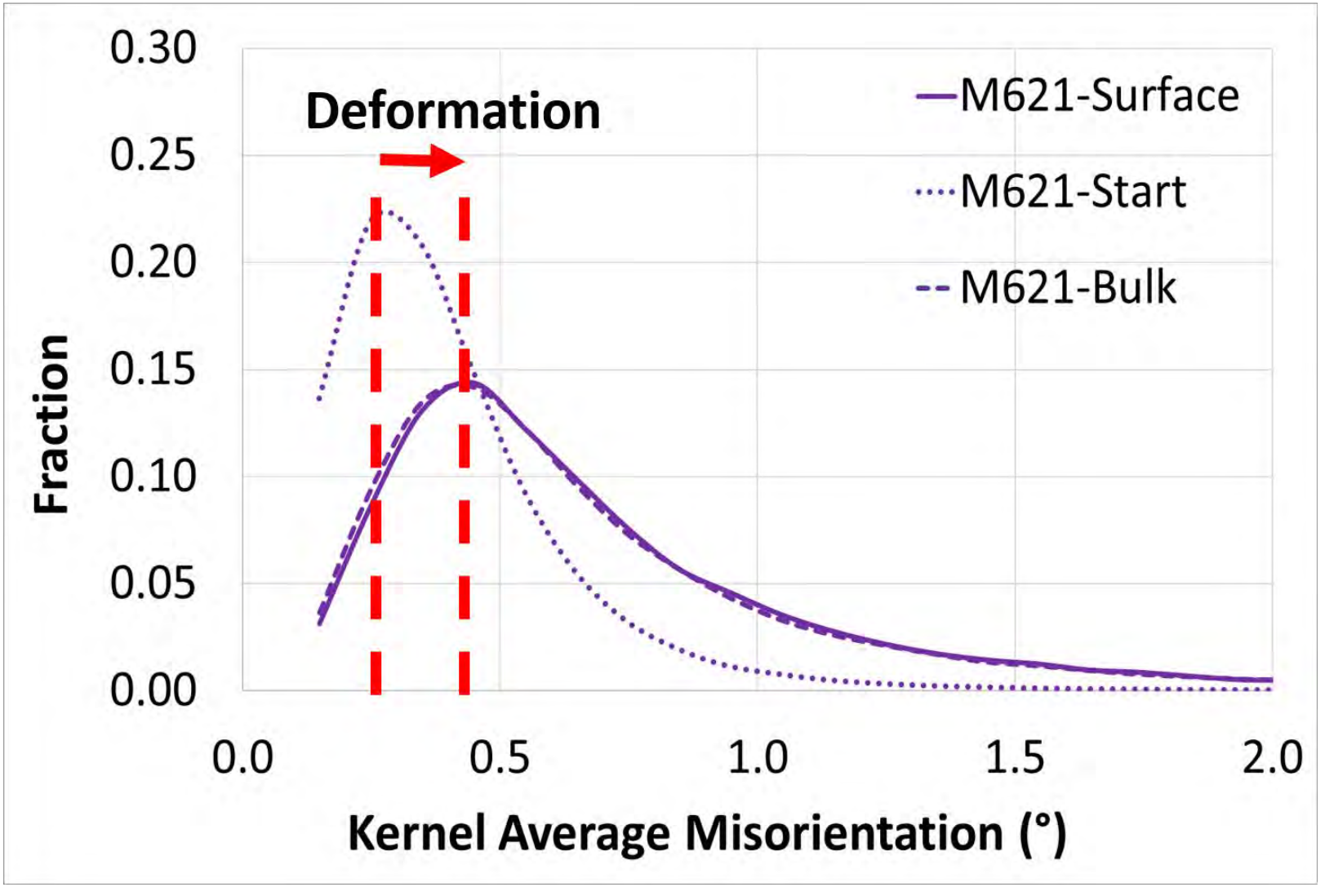
Deformation
M621-Surface
M621-Start
M621-Bulk
Fraction
0.30
0.25
0.20
0.15
0.10
0.05
0.00
0.0
0.5
1.0
1.5
2.0
Kernel Average Misorientation (°)

Figure 9

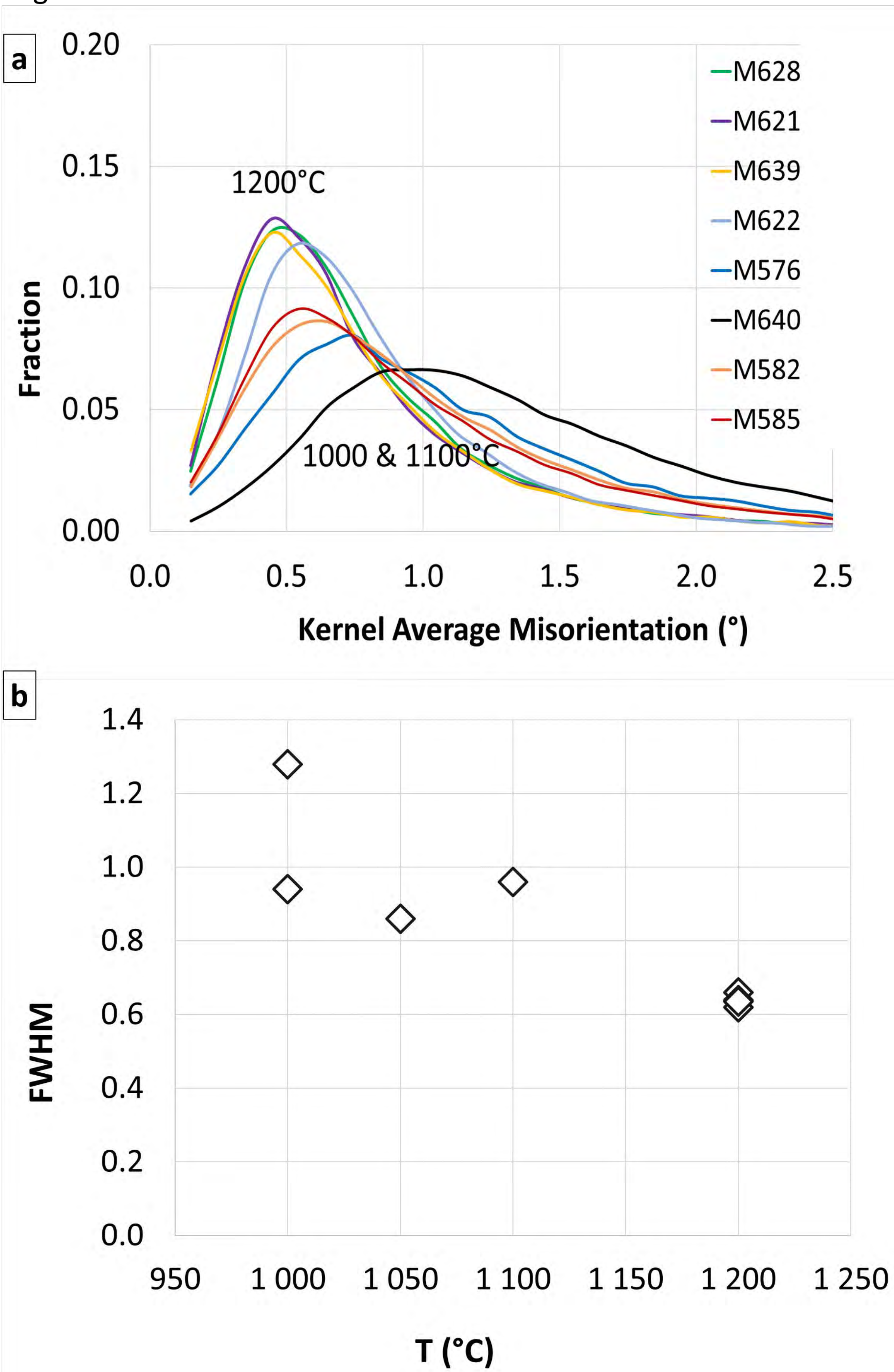
a
0.20
0.15
0.10
0.05
0.00
Fraction
1200°C
1000 & 1100°C
M628
M621
M639
M622
M576
M640
M582
M585
0.0
0.5
1.0
1.5
2.0
2.5
Kernel Average Misorientation (°)
b
1.4
1.2
1.0
0.8
0.6
0.4
0.2
0.0
FWHM
950
1 000
1 050
1 100
1 150
1 200
1 250
T (°C)

1050°C M585

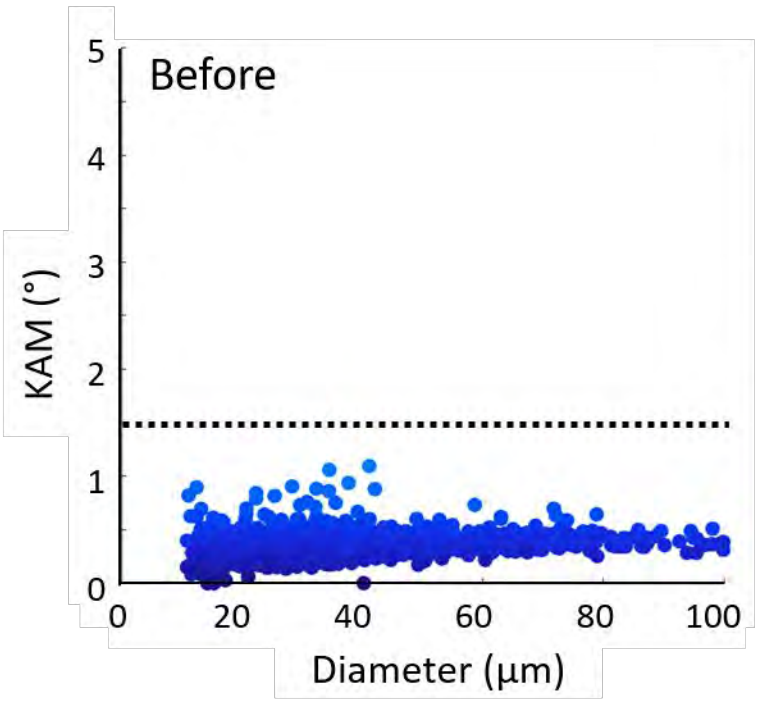

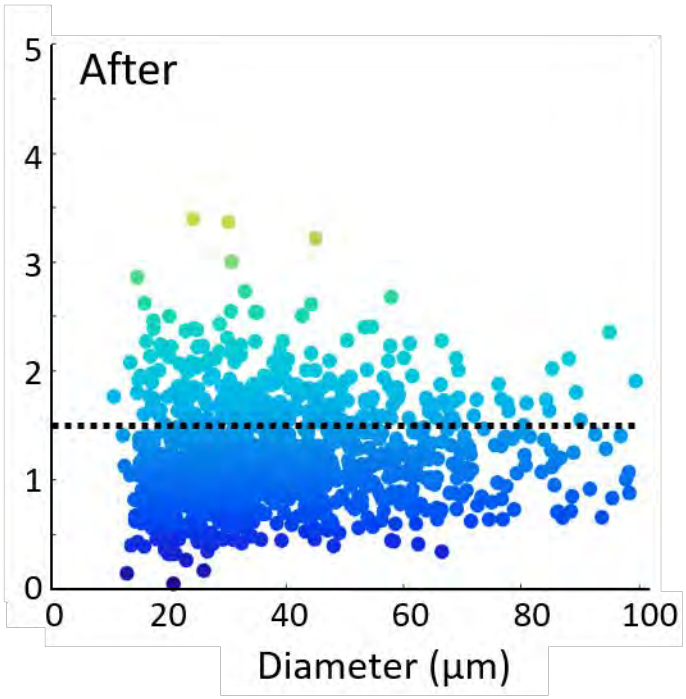

1000 °C M582

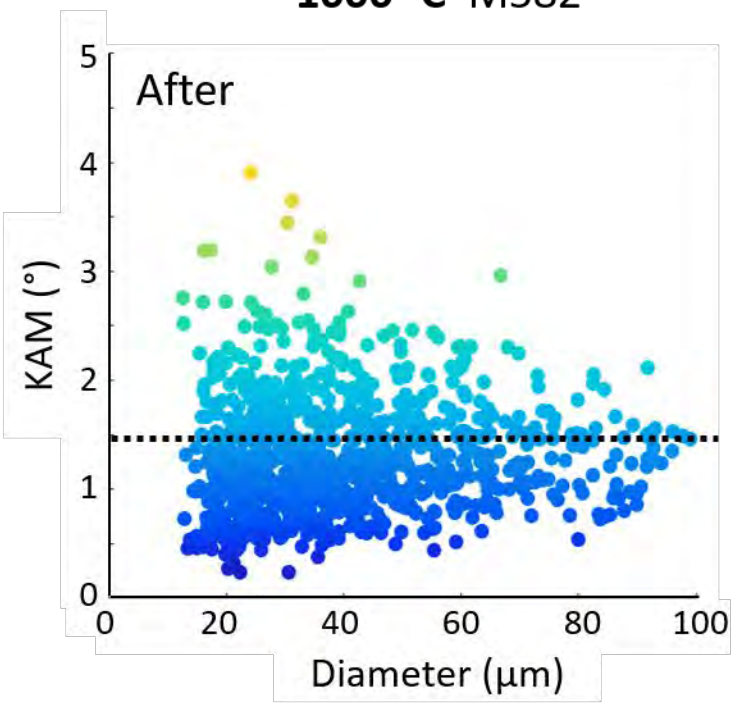

1200°C M628